




FACULTY OF SCIENCE AND TECHNOLOGY

MASTER'S THESIS

Study program/ Specialization: Offshore Field Development Technology/ Marine and Offshore Technology	Spring semester, 2021 Open
Author: Ivantsiv Alexey	 (author signature)
Tutor: Associate Professor Knut Erik Teigen Giljarhus	
Master thesis title: Исследование надежности участка морского трубопровода на основе моделирования вибраций, вызванных внешним потоком	
English title: CFD analysis of subsea pipelines and risers.	
Keywords: Marine riser, oscillating cylinder modelling, VIV analysis, multistrip method, riser bending stress.	Number of pages: 77 + appendices/other: Stavanger, June 15, 2021 date/year

Abstract

In the master's thesis, an analysis of promising shelf areas in Russia is given for the need to introduce riser systems. The main risers types used in the oil and gas industry are described.

The global tasks in work are the study and modelling of cylinder vibrations, the fluid-structure interaction, the combination of hydrodynamic and structural dynamics approaches to investigate the reliability of a marine riser under certain conditions.

The study of the dynamic behavior of the riser in the flow has been carried out. The calculation of the loads to which the riser is subjected is presented. The displacement amplitudes and frequency characteristics are analyzed.

The work done via the multistrip method to calculate the structural dynamics of the riser based on two-dimensional modelling of the cylinder vortex-induced vibration in the flowing stream. Modal analysis was performed to find the natural frequencies and response frequencies to determine the riser shape.

Acknowledgements

I would like to express appreciation to Associate Professor Knut Erik Teigen Giljarhus for sharing valuable materials needed for the master thesis work.

Thanks a lot to Prof. Muk Chen Ong for sharing knowledge in marine operations and aspect related to the VIV problems. I also value the insights related to the pipelines and risers provided by Professor Daniel Nalliah Karunakaran during the lectures at the university.

Many thanks to my wife and parents for their great support while I was working on this master thesis.

Alexey Ivantsiv
June 2021
Stavanger, Norway



Acronyms and Abbreviations

LES	Large Eddy Simulation
DES	Detached Eddy Simulation
DNS	Direct Numerical Simulation
RANS	Reynolds-Averaged Navier-Stokes equations
SPA	Spalart–Allmaras turbulence model
SST	Shear Stress Transport
VIV	Vortex-Induced Vibrations
SCR	Steel Catenary Risers
TTR	Top Tensioned Riser

Table of Content

Abstract.....	i
Acknowledgements.....	ii
Acronyms and Abbreviations	iii
List of Figures.....	vii
List of Tables	ix
List of Symbols.....	x
1 Introduction	1
1.1 Motivation.....	1
1.2 Riser definition	1
1.2.1 Steel Catenary Risers	3
1.2.2 Top Tensioned Risers	3
1.2.3 Flexible Risers	3
1.2.4 Hybrid Risers	4
1.3 Materials used in risers manufacturing.....	4
1.3.1 Steel pipes	5
1.3.2 Flexible pipes.....	5
1.4 Environmental conditions description	7
1.4.1 Prospective offshore oil and gas bearing areas in Russia.....	7
1.4.2 Characteristics of the South Barents Basin.....	9
1.5 Importance of VIV analyses for risers	11
2 Hydrodynamics Basics	13
2.1 Flow Regimes	13
2.1.1 Laminar Flow.....	13
2.1.2 Turbulent Flow	14
2.2 Turbulence models.....	15
2.2.1 Near-wall layer	16
2.2.1.1 Laminar boundary layer	17
2.2.1.2 Turbulent boundary layer.....	19
2.2.1.3 The law of the wall.....	21
2.2.2 Direct Numerical Simulation.....	24
2.2.3 Large Eddy Simulation.....	24
2.2.4 Detached Eddy Simulation	24

2.2.5	Reynolds-Averaged Navier-Stokes equations	25
2.2.5.1	Spalart–Allmaras turbulence model	27
2.2.5.2	k- ϵ model	28
2.2.5.3	k- ω model	29
2.2.5.4	k- ω SST model	30
3	Vortices and Vibrations	31
3.1	Vortex (Eddy) Definition	31
3.2	Vortex Shedding Mechanism	32
3.3	Vortex Shedding After Fixed Cylinder	35
3.4	Vortex-Induced Vibrations	37
3.4.1	VIV Principle	37
3.4.2	Key Parameters	38
3.4.2.1	Reynolds Number	39
3.4.2.2	Strouhal Number	39
3.4.2.3	Frequencies Definition	40
3.4.2.4	Lock-In Conditions	41
3.4.2.5	Reduced Velocity	42
3.4.2.6	Mass Ratio	43
4	Oscillating Cylinder Model Description	45
5	Structural Dynamics	49
5.1	Modal Analysis	49
5.1.1	Determination of Natural Frequencies	50
5.1.2	Real Response of the Riser	51
5.2	Riser Shape Determination	51
5.3	Stresses Calculations	53
5.3.1	Von Mises Criterion	53
5.3.2	Maximum Bending Stress	57
6	Modelling and Calculations	58
6.1	Input data	58
6.2	Choosing the riser type	58
6.3	Diameters calculation	59
6.4	Frequency analysis	60
6.5	Cylinder Oscillation Modelling	62
6.5.1	Input parameters	62
6.5.2	Modelled Domain	63

6.5.3	Mesh Generation.....	64
6.5.4	Modelling Results.....	65
6.6	Riser Shape Determination.....	68
6.7	Bending Stress Calculation.....	71
	Discussion.....	73
	Bibliography.....	75

List of Figures

1.1.	Schematic representation of the riser	2
1.2.	Typical cross-section of flexible pipe (Yong Bai, Qiang Bai, 2014)	5
1.3.	Overview map of Kara and Barents seas	8
1.4.	Current velocity profile (Park et al., 2020)	10
1.5.	Current velocity profile along the riser	11
2.1.	Laminar flow: a) stream lines; b) velocity profile	14
2.2.	Turbulent flow: a) stream lines; b) velocity profile	14
2.3.	Schematic comparison of turbulence models (Heng X., Paola C. 2019)	16
2.4.	Uniform flow along the surface of a flat plate (Çengel Y.A. and Cimbala J.M., 2010)	17
2.5.	Laminar flow velocity profile (Çengel Y. A. and Cimbala J. M., 2010)	18
2.6.	Turbulent flow velocity profile (Çengel Y. A. and Cimbala J. M., 2010)	21
2.7.	Law of the wall in the turbulent boundary layer	23
3.1.	Schematic view on the vortex	31
3.2.	Flow structure at the boundary surface	32
3.3.	Pressure system around the fixed cylinder	33
3.4.	Detailed picture of flow near to separate (Sumer B., Fredsoe J., 2006)	34
3.5.	Vortex forming (Sumer B., Fredsoe J., 2006)	34
3.6.	Vortex shedding after the cylindrical body	35
3.7.	Cylinder vibration principle	38
3.8.	Strouhal-Reynolds number relationship (Zahari M.A., Dol S.S, 2015)	40
3.9.	Lock-In conditions at specific reduced velocities (Sumer B., Fredsoe J., 2006)	43
4.1.	Schematic representation of oscillating cylinder system	46
4.2.	Types of damped oscillations	48
5.1.	The equilibrium conditions representation (Karunakaran D.N., 2020)	54
5.2.	Axial stress decomposition	56
6.1.	Schematic representation of the task	59
6.2.	Modelled Domain	63
6.3.	Detailed mesh view: a) in near-wall layer, b) around the cylinder	65
6.4.	Flow development in the wake	66
6.5.	One vorticity zone cuts another	66
6.6.	Vorticity intensity dissipation	66

6.7. Velocity field around cylinder and in the wake (at surface)	67
6.8. Lift coefficient distribution in time	67
6.9. Drag coefficient distribution in time	68
6.10. Riser displacement in direction: a) in-line (X) and b) cross-flow (Y)	71

List of Tables

1.1. Distribution of initial total resources (ITR) over the seas of the Russian Federation.	7
1.2. Main characteristics of deposits in the South Barents basin.	10
6.1. Input data.	58
6.2. Riser parameters.	59
6.3. Eigenfrequencies for certain mode.	62
6.4. Boundary conditions for pressure and velocity.	64
6.5. First layer thickness determination.	64

List of Symbols

$\overline{F}_D, \overline{F}_L$ – drag and lift forces

C_D, C_L – drag and lift coefficient

F_τ – shear force

R_{min} – minimal radius of curvature

U_r – reduced velocity

f_n – natural frequency

f_{osc} – oscillating frequency

f_v – vortex shedding frequency

m^* – mass ratio

$\ddot{x}, \dot{x}, x, \ddot{y}, \dot{y}, y$ – acceleration, velocity and displacement of cylinder in x and y directions

μ_t – turbulent viscosity

c – damping coefficient

C_a – added mass coefficient

D – cylinder diameter

E – Young's modulus

f_1, f_3 – design factors

I – area moment of inertia

$k(z)$ – pipe curvature

L – length

M – mass per unit length

m_a – added mass

n – mode number

r_o – pipe outside radius

T – averaged tension

t – pipe wall thickness

U – free stream velocity

ν – Poisson ratio

ε_{max} – relative deformation of pipe

ρ – medium density

σ_b – bending stress

σ_{ec} – end-cap stress

σ_{eq} – equivalent stress

σ_h – hoop stress

σ_l – longitudinal stress

σ_t – thermal stress

σ_y – yield strength

$\Phi''(z)$ – pipe shape

A – contact area

Re – Reynolds Number

St – Strouhal Number

k – stiffness

m – cylinder mass

p – pressure

u – velocity

ν – kinematic viscosity

μ – dynamic viscosity

τ – shear stress

Chapter 1

1 Introduction

1.1 Motivation

Risers are essential components of offshore operations as they are the link between the seabed and the surface, be it drilling or production. Risers are subjected to various types of loads: waves, deep-sea currents, platform movement on the ocean surface.

Constant and cyclic loads, as well as fatigue of materials to the development of mechanical damage. When submerged underwater, pipes are also subject to vortex-induced vibrations that require performance requirements.

Analysis of vortex-induced vibrations is an important aspect when designing a field development using risers.

First of all, it is necessary to make sure that there are no resonance conditions in which the amplitudes of vibrations, or in other words, displacements, increase sharply. Under these conditions, bending the riser in certain areas may cause the stress in the riser to exceed the maximum allowable stress for that type of riser.

In addition, even if the stresses are not immediately exceeded due to the increases in displacement amplitudes, cyclic intense loads can lead to a rapid accumulation of fatigue, which ultimately will still lead to an accident.

It will be much cheaper and safer to spend a certain amount of resources at the design stage than to find an unacceptable riser configuration for which the effects of vibrations are critical.

Thus, researching modelling and calculation is essential even before the riser is placed under operating conditions.

1.2 Riser definition

The riser is the pipe that connects the subsea equipment to the topside (Fig. 1.1). It is widely used for deepwater fields where a water depth is about 500 meters and more. At the same time, such a system may be suitable for shallow water if the water is deep enough to make direct contact with the seabed impossible.

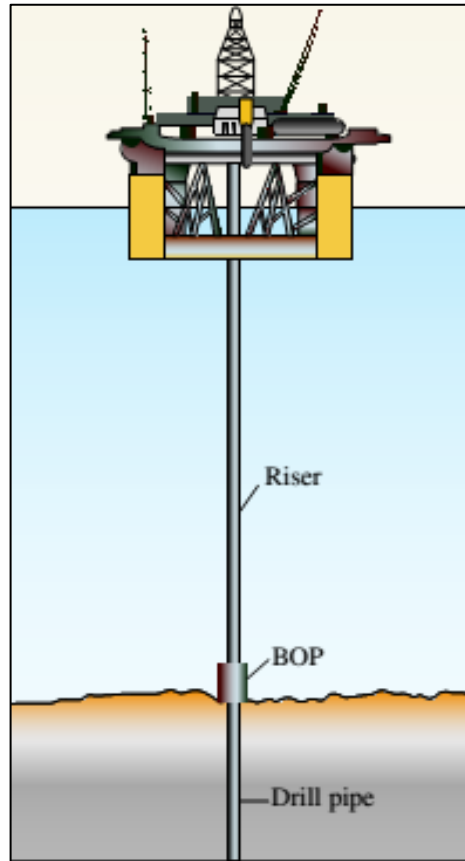


Fig. 1.1. Schematic representation of the riser

According to the main purpose of their implementation, the risers can be divided into the following groups:

- Production;
- Drilling;
- Export of oil and gas;
- Water/gas injector.

In addition, all risers are classified as flexible or rigid. Which riser type will be selected depends on the field geometry, seabed conditions, development concept and is validated through stress analysis and simulation.

The main types of risers used in oil and gas industry:

- Steel Catenary risers;
- Top tensioned risers;
- Flexible risers;
- Hybrid risers.

1.2.1 Steel Catenary Risers

Steel catenary risers are free-hanging tubes with no intermediate buoys or floating devices. This type of riser is located horizontally at the lower end and usually within 20 degrees of vertical at the upper end. In this shape, the riser is an extension of the flow line that is suspended from the platform. Flexible joints can be used to provide relative rotational motion between the riser and the platform. (Yong Bai, Qiang Bai, 2019)

This type of risers is a very good solution for oil and gas export and water injection lines in fields located in deep water where flexible risers are technically and economically limited.

Steel catenary risers are sensitive to waves and currents due to their usually low effective stress. Fatigue damage caused by vortex vibrations can be fatal for such a pipe. The use of suppression devices such as propeller struts and fairing can help reduce vibration to an acceptable level.

1.2.2 Top Tensioned Risers

Tensioned risers are long, circular pipes used to connect the seabed to a floating platform. They were designed for use in shallow water, but the need for new designs increases as the water depth increases.

These risers are exposed to constant currents of varying intensity and oscillatory wave currents. These pipes are fitted with a top tensioning system to maintain a constant deflection angle at the upper and lower ends despite external loads. The tension requirements for production risers are generally lower than for drilling risers.

For the stability of this type of risers, a suspension tensioner is used that exceeds their apparent weight. Top Tension Risers are typically used on tension leg platforms or SPAR type platforms. The riser is supported by a platform using hydropneumatic devices that allow the pipe to move axially or move relative to the platform at the surface. (Yong Bai, Qiang Bai, 2019)

1.2.3 Flexible Risers

Flexible risers are multilayer composite pipes with a specific bending resistance that ensures stability in a given configuration. They have become a successful solution for deep and shallow water worldwide.

Flexible risers are the result of a unique development program based on flexible pipes. It has been found that this type of pipe is ideal for offshore applications in production and export lines. (Yong Bai, Qiang Bai, 2019)

1.2.4 Hybrid Risers

The hybrid riser concept was developed based on the tensioned riser. Its main feature is that it allows relative movement of the floating structure and the rigid metal riser, connecting them with flexible jumpers (Yong Bai, Qiang Bai, 2019).

The main elements of the hybrid riser are:

- Peripheral lines;
- Subsea foundation;
- Tensioned riser;
- Floating module;
- Flexible pipes.

Peripheral production and export lines are led to the submarine base, where they are supported by additional floating modules to allow them to move freely in the axial direction.

The base has devices for connecting peripheral lines with a tension riser. The riser itself is secured to the subsea foundation with a hydraulic connector and vertically positioned due to the tension created by the main floating module.

A flexible pipe is attached to a tensioned riser at its upper end and connects the subsea system to the surface operating unit, compensating for relative movements.

1.3 Materials used in risers manufacturing

As mentioned earlier, risers are divided into flexible and rigid. Rigid ones mean risers made from various types of steels. On the other hand, flexible pipes are a configurable product made up of multiple layers of materials.

The choice of material for a particular object is based on the analysis of numerous input parameters such as:

- Geography of the deposit;
- Chemical composition of external and internal fluid;
- Project design of the riser;
- The time frame of operation.

In addition, some guidelines and regulations establish requirements for the main parameters of pipes and risers used in subsea production. (GOST 33005 (ISO 13625), GOST R 54382, DNV OS-F101, DNVGL-SE-0476)

1.3.1 Steel pipes

The steels used in the marine industry typically contain up to 0.5% carbon and can be alloyed in several ways to achieve the desired properties.

The pipe materials used for steel risers are usually selected from a range of welded or seamless carbon steel pipes. Quality standards for pipe production vary from country to country. Examples of Russian and foreign standards: GOST R ISO 10332-99, API 5L, ISO 13624-1.

If to talk about steel risers, the most famous materials are steel grades X60, X65, X70, X80. However, today there is a rapid development of technologies to produce pipes from more specific titanium and aluminium alloys.

1.3.2 Flexible pipes

Flexible pipes are a modular design (Fig. 1.2) in which the layers are independent but designed to interact with each other. It means that each layer can be tailored to its intended use and independently adjusted to meet specific field development requirements.

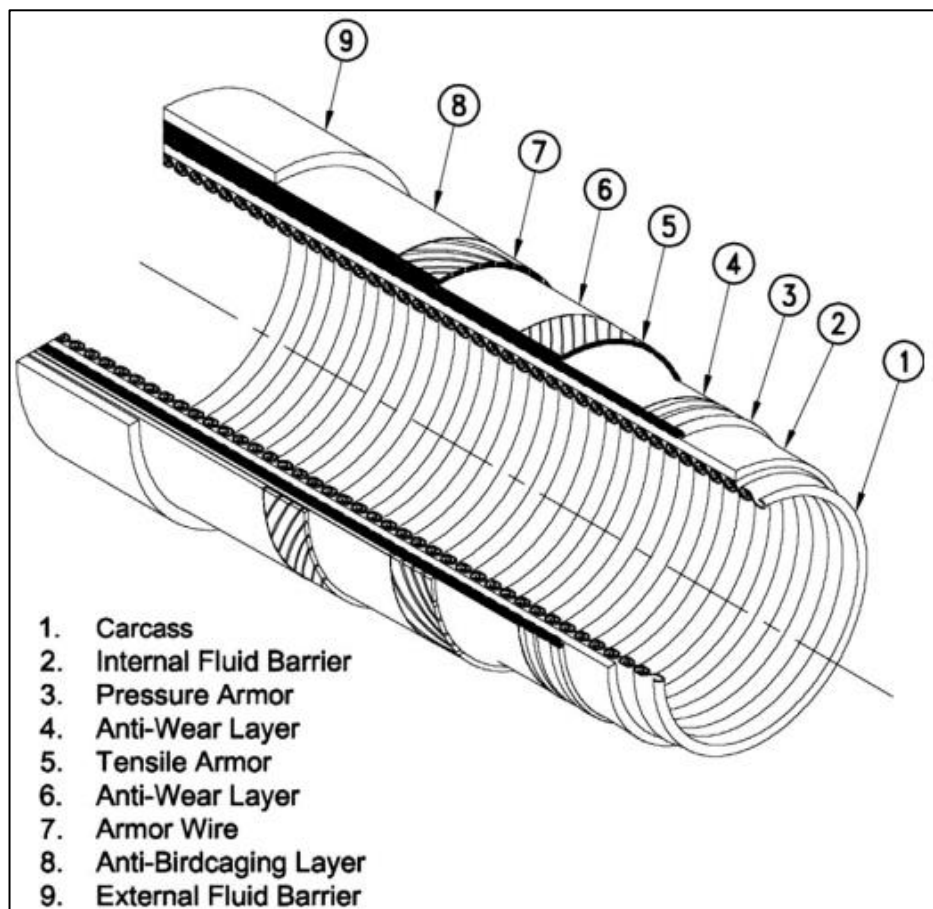


Fig. 1.2. Typical cross-section of flexible pipe (Yong Bai, Qiang Bai, 2014)

The main components for flexible pipes are hermetically sealed thermoplastic barriers and corrosion-resistant steel. The spirally wound steel wire gives the pipe high-pressure resistance and characteristics for flexibility and excellent dynamic behavior.

There are two types of coiled tubing: bonded and unbonded coiled tubing. In bonded pipes, the different layers of elastomer and steel are bonded together through a vulcanization process. Bonded pipes are used for short sections only. However, flexible pipes without bonding can be made for dynamic applications with a length of several hundred meters. (Yong Bai, Qiang Bai, 2014).

The carcass forms the innermost layer of the cross-section of the flexible pipe. Usually made of a flat stainless steel strip that forms a blocking profile. The primary function of the frame is to prevent pipe collapse due to hydrostatic pressure or gas build-up in the annulus. (Yong Bai, Qiang Bai, 2014)

The inner polymer jacket provides a barrier to maintain fluid integrity in the wellbore. Exposure concentrations and fluid temperature are critical factors in determining core design. The materials used for the inner shell can be polyamide-11, high-density polyethylene. (Yong Bai, Qiang Bai, 2014)

The role of the pressure armor is to withstand the hoop stress in the pipe wall caused by the internal fluid pressure in the barrel. The armor is wound on an inner polymer sheath and made of connecting wires. (Yong Bai, Qiang Bai, 2014)

The layers of elastic armor are always wound in pairs. As their name suggests, these layers of armor are used to resist the tensile load on the flexible pipe. They are used to support the weight of all pipe layers and transfer the load through the end fitting to the structure. High stress in a marine riser may require four layers of tensile armor rather than two. (Yong Bai, Qiang Bai, 2014)

The outer polymeric shell can be made from the same materials as the inner polymeric shell. The primary function of the outer shell is to protect against seawater. It also provides an adequate level of protection for the pipe against a collision with other objects during installation. (Yong Bai, Qiang Bai, 2014)

In addition to the five primary layers of coiled tubing, there are additional layers. These layers include anti-friction tapes wrapped around the armor layers that reduce the friction and wear of the wire layers as they rub against each other when the pipe is bent due to external stress. In addition, anti-wear belts ensure that the shape of the winding of the armor layers is maintained.

These layers also prevent the pre-set wire from twisting. A phenomenon called birdcage, which results from hydrostatic pressure causing axial compression in the pipe. (Yong Bai, Qiang Bai, 2014)

Some flexible tubing applications require the use of high tensile wire to provide tissue elongation observed due to high tensile loads.

Yet, the presence of an oxidizing marine environment results in these pipes having unacceptable wear resistance. The solution to this situation is to manufacture the pipe cross-section with two separate winding rings rather than one.

1.4 Environmental conditions description

The use of risers is associated with offshore fields, developed by production units that do not directly contact the bottom when the depths are large enough to exclude the possibility of development utilizing platforms on a gravity basis.

The topography of the seabed and the soil properties may also be a reason to make installing the platform on the bottom impossible. It may do not meet the requirements of safety and environmental friendliness.

Furthermore, loads from the weight of the foundation and platform can cause ground movement. In addition, due to the enormous construction costs, it is not always economically profitable to use this approach when designing a development.

Thus, riser studies should be carried out for the conditions of offshore fields, which today are promising in terms of reserves and are located in areas with a depth sufficient for the introduction of risers.

1.4.1 Prospective offshore oil and gas bearing areas in Russia

Offshore production in Russia was not of much interest until the 2000s, as there was a massive reserve of onshore fields. At the same time, the level of technology did not allow economically developing complex areas at that time. However, the situation has changed in recent years.

Currently, offshore fields are being actively introduced into the development stage. At the same time, Russia possesses impressive reserves classified as fields that have not yet been commissioned for one reason or another.

Table 1.1 shows the distribution of the initial total resources across the seas of the Russian Federation.

Table 2.1. Distribution of initial total resources (ITR) over the seas of the Russian Federation (Grigorenko Y.N. et al., 2007)

№	Seas of Russian Federation	ITR, %
	Total 100 %, geological	100 %

№	Seas of Russian Federation	ITR, %
1	Kara sea (offshore)	31.6 %
1a	Kara sea (bays)	5.8 %
2	Barents sea	19.8 %
3	Okhotsk sea	11.0 %
4	Pechora sea	8.1 %
5	East-Siberian sea	7.0 %
6	Caspian Sea	4.6 %
7	Chukchi sea	4.2 %
8	Laptev sea	3.7 %
9	Bering Sea	1.4 %
10	Black Sea	1.4 %
11	Japanese Sea	0.7 %
12	Azov sea	0.5 %
13	Baltic Sea	0.1 %
14	Pacific Ocean	0.1 %

According to work (Grigorenko Y.N. et al., 2007), more than half of the marine reserves are located in the Kara and Barents Seas. However, if we study the overview map of these seas (Fig. 1.3) for depths, we can conclude that for the Kara Sea deposits, the most typical depths are in the range of 25-100 meters; for fields in the water area of the Barents Sea 25-300 m.

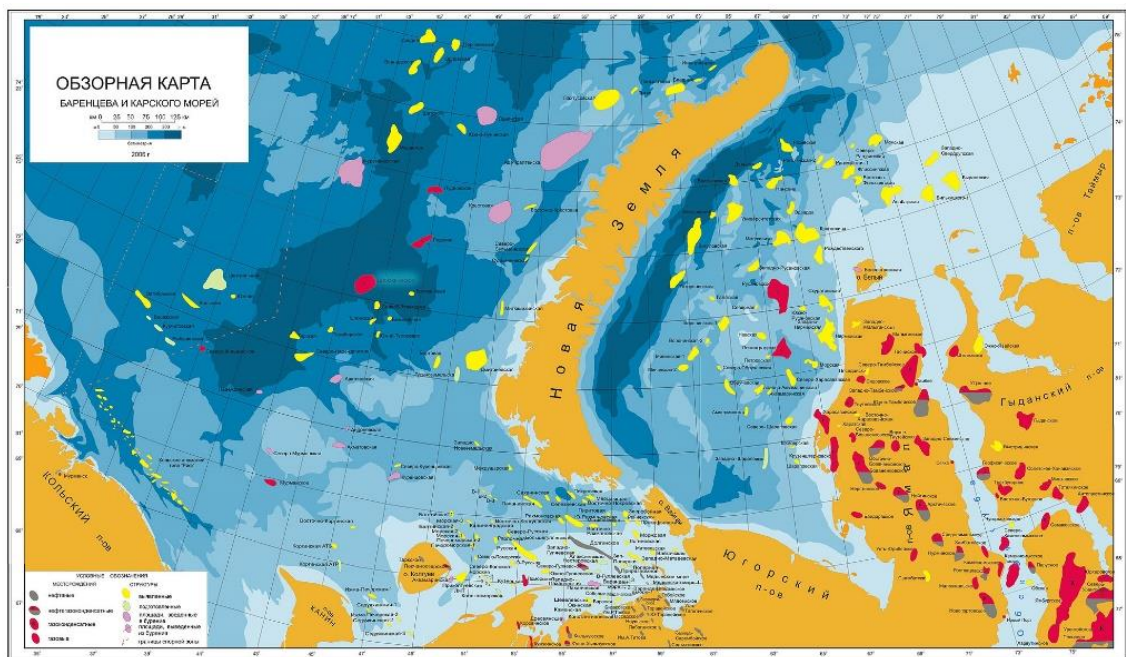


Fig. 1.3. Overview map of Kara and Barents seas

If we consider the most famous and large fields, for which the depths are more consistent with the depths of the use of risers, then the Barents Sea comes to the fore. Thus, the studies presented in this work will be carried out for the conditions of the oil and gas-bearing area of the Barents Sea, which is distinguished into an independent South Barents basin.

1.4.2 Characteristics of the South Barents Basin

Five fields have been discovered in the South Barents basin:

- Severo-Kildinskoye;
- Murmanskoe;
- Shtokman;
- Ledovoe;
- Ludlovskoe.

The Severo-Kildinskoye field is located 325 km from the city of Murmansk - the nearest ice-free seaport and railway station. The depth of the sea in the area of the field is 230-280 m. Therefore, it is small in terms of reserves.

The Murmanskoe gas field is confined to a local structural uplift formed above the system of disturbances in the southwestern edge of the basin. The depth of the sea within its limits varies from 68 to 123 m. By the amount of geological gas reserves, the Murmanskoe field is classified as large.

The Shtokman gas condensate field is located in the northwestern marginal part of the South Barents Basin in the central part of the Barents Sea, within the edge terrace, approximately 600 km northeast of Murmansk. The sea depths in the area of the field range from 279 to 380 m. The Shtokman field is classified as unique in terms of geological gas reserves.

The Ledovoe gas condensate field is located in the northeastern part of the Barents Sea, 70 km northeast of the Shtokman field and is confined to a very large structure. The sea depth in the area of the field is 200-280 m. Two wells have been drilled in the field. According to preliminary estimates regarding its geological gas reserves, the Ledovoe field is classified as a large field.

The Ludlovskoye gas condensate field is located 50 km north of the Ledovoye field, within the Ludlovskoye Uplift, limiting the South Barents Basin in the central part of the Barents Sea of the Russian Federation. Within the area of the field, the sea depth is 200-240 m. The Ludlovskoye field, in terms of the amount of geological gas reserves, belongs to large fields.

The basin has impressive gas reserves and is very promising. The characteristics of the deposits in this basin, presented at the conference in 2012 (Kulpin L.G. et al., 2012), are shown in Table 1.2.

The fields of the South Barents Basin, with the exception of the Murmansk one, are characterized by depths of more than 200 m. Therefore, it suggests that it is necessary to implement solutions based on floating operating units for their development. Consequently, using risers to connect subsea devices or a wellhead with a floating unit will become one of the primary links in a development project.

Table 1.2. Main characteristics of deposits in the South Barents basin (Kulpin L.G. et al., 2012)

Characteristics	Gas-bearing fields				
	Severo-Kildinskoye	Murmanskoe	Ledovoe	Ludlovskoye	Shtokman
Reserves, billion m ³	15,6	120,6	422,1	211,2	3900
Size category	Small	Large	Large	Large	Unique
Area, km ²	330	340	390	940	960
Water depths, m	240	120	200	250	350

Thus, it can be sad that the analytical calculation of the loads on the riser for the conditions of the fields in the South Barents basin will be helpful for further design work.

To perform the analysis, metocean data on the current velocity characteristic of the territory of this basin are required. In this work, the analysis of extreme values of metocean data for the Barents Sea (Park et al., 2020) results was used.

In studies (Park et al., 2020), the distribution of the current velocity in the direction of depth (z) is presented (Fig. 1.4). In this case, the current velocity profile was transformed to a dimensionless value taking into account the water depth in the field area (d).

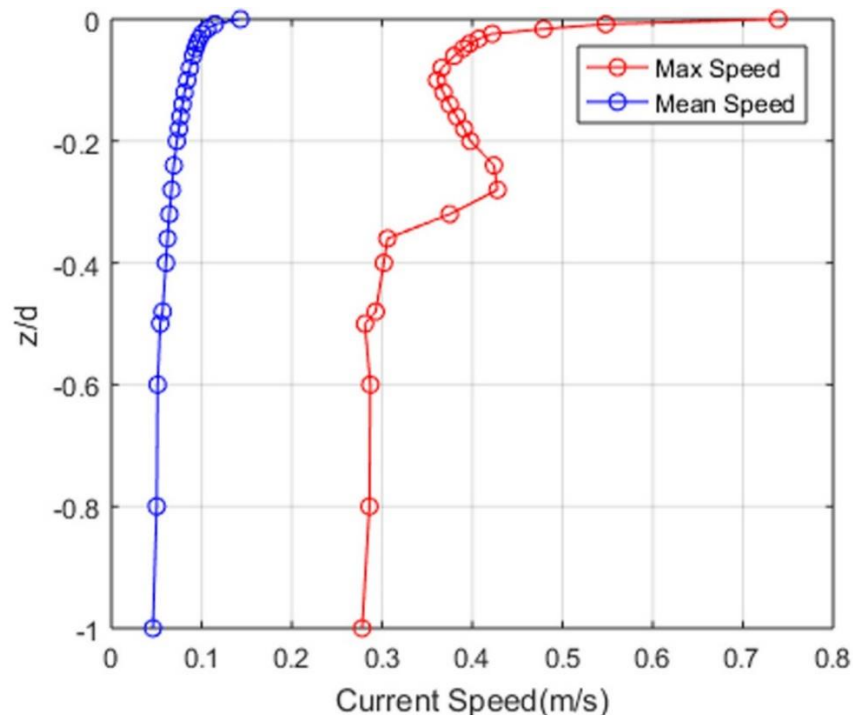


Fig. 1.4. Current velocity profile (Park et al., 2020)

Such data presentation allows this dependence to be used for any depth, assuming a proportional change in the velocity profile.

For mean and maximum current velocity profiles, the highest values are related to surface conditions. There is also an uneven decrease in speed with depth. A layer is distinguished at a certain depth from the surface, which has an increased, relative to neighbouring layers, maximum flow rate.

1.5 Importance of VIV analyses for risers

When the incident flow is flowing around a cylindrical surface, vortices are formed on both sides of the cylinder. The inconsistency of the vortices leads to the periodicity of the action of hydrodynamic forces. It makes the cylinder to oscillate both in the direction of the flow and in the direction perpendicular to it. This phenomenon is called vortex-induced vibration (VIV).

Vibrations occur when the pipe is not fixed or supported and can move through the medium. Such conditions are typical for pipelines located at the bottom of the sea. In turn, vibrations can lead to a rapid accumulation of fatigue damage and an increase in frontal loads on thin structural elements. So, it should be taken into account during the design phase of subsea pipelines.

Vibration stress can significantly shorten the life of a structure. Stretching, compression and bending caused by the oscillatory movement of the pipe leading to steel fatigue and, as a result, to failure.

It is evident to the risers that they are flowing along their entire length. Moreover, the flow rate varies with water depth (Fig. 1.5).

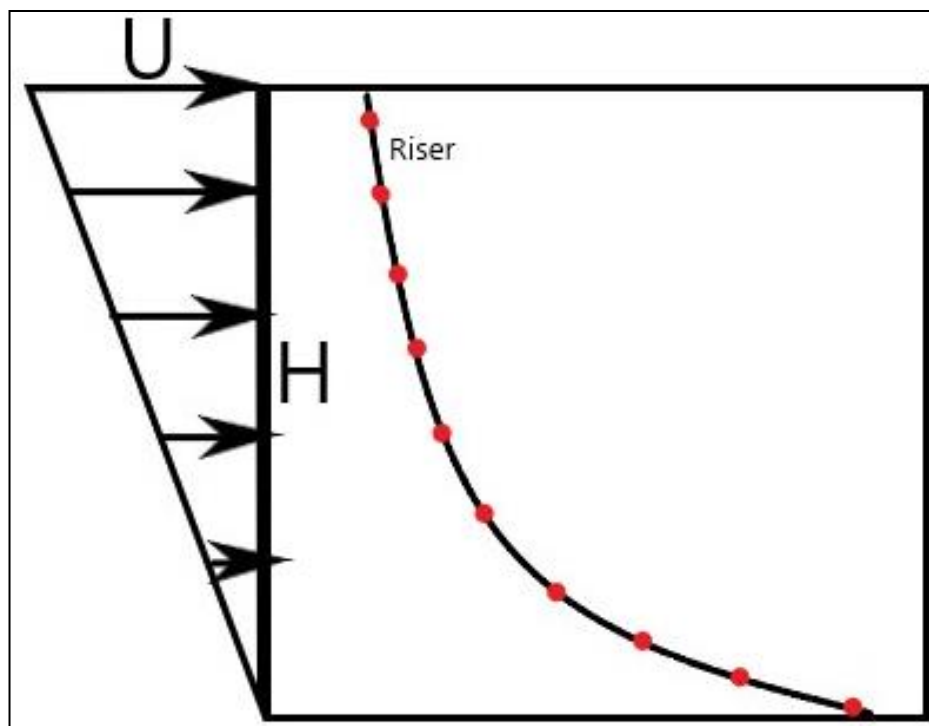


Fig. 1.5. Current velocity profile along the riser

Each individual point taken along the length of the riser corresponds to its own value of the flow velocity. It leads to the appearance of many natural frequencies and possible response frequencies.

When solving this problem, a dimensionless frequency is used to determine potential excited modes. The found potential modes and natural frequencies are used to analyze the oscillatory movements of the studied riser under specified conditions. The analysis is carried out to identify possible areas of the pipeline in which conditions arise to reach the critical values of the amplitudes and resonant frequencies of oscillations to design the riser to be safe.

Vortex-induced vibrations are a hazardous factor for risers since additional forces of influence can lead to exceeding the permissible stress values. Furthermore, if the effect of vibrations was not considered, the curvature of the riser can exceed the permissible values and cause its destruction or leakage. The analysis and research presented in this work allow assessing these risks and finding ways to avoid negative consequences.

Chapter 2

2 Hydrodynamics Basics

First of all, when studying a marine riser dynamic in the seawater environment, it is necessary to formulate a mathematical problem that describes the behavior of the environment itself. For this, both fundamental concepts and equations of hydrodynamics are used and more specific equations characterizing the effects of turbulence and the interaction of the flow with the walls of an object placed in the path of the flow.

2.1 Flow Regimes

The flow regime is an essential aspect in predicting flow behavior since its parameters can vary significantly when changing from one flow regime to another. In addition, a particular flow regime corresponds to its own physical processes, which are mathematically described in different ways.

The transition from laminar to turbulent regime occurs when the so-called critical Reynolds number Re_{cr} is reached. At $Re < Re_{cr}$, the flow occurs in a laminar regime, at $Re > Re_{cr}$, turbulence may arise.

First of all, the critical value of the Reynolds number depends on the specific type of flow (flow in a circular pipe, flow around a ball), but, in addition, on many parameters of both the flow itself and the streamlined body example, surface roughness.

It should also be noted that the process of transition from laminar to turbulent flow regime is not instantaneous. As a result, a transient flow regime is also distinguished.

2.1.1 Laminar Flow

Laminar flow is a flow in which fluid moves in layers without mixing and pulsations (random rapid changes) of velocity and pressure.

Below is a graphical representation of streamlines (Fig. 2.1a) and velocity profile (Fig. 2.1b) for laminar flow between two walls.

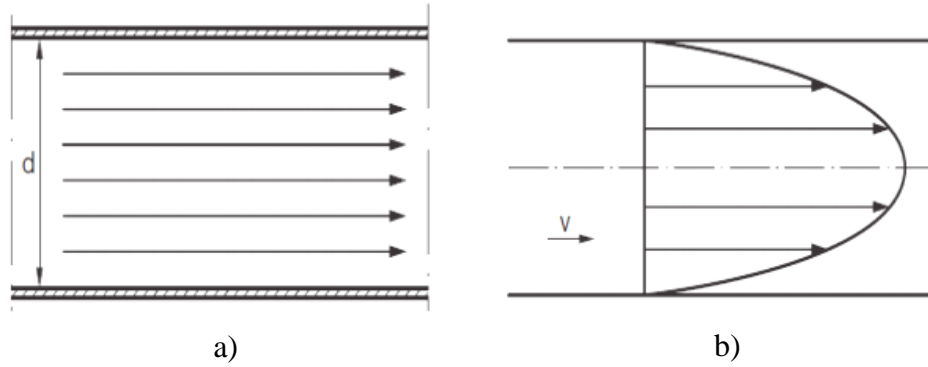


Fig. 2.1. Laminar flow: a) stream lines; b) velocity profile

In fully developed laminar flow, each fluid particle moves at a constant axial velocity along the streamline, and the velocity profile remains unchanged in the flow direction.

There is no movement in the radial direction. Therefore the velocity component in the direction normal to the pipe axis is zero everywhere (Çengel Y. A. and Cimbala J. M., 2010).

In a laminar flow, the velocity changes with distance from the wall according to a parabolic law.

2.1.2 Turbulent Flow

Turbulence is a phenomenon consisting of the spontaneous formation of numerous nonlinear fractal waves and ordinary, linear waves of various sizes without the presence of external, random forces that disturb the environment.

Turbulent flow is characterized by random and fast oscillations of swirling areas of the liquid (Fig. 2.2a), called vortices. (Çengel Y. A. and Cimbala J. M., 2010)

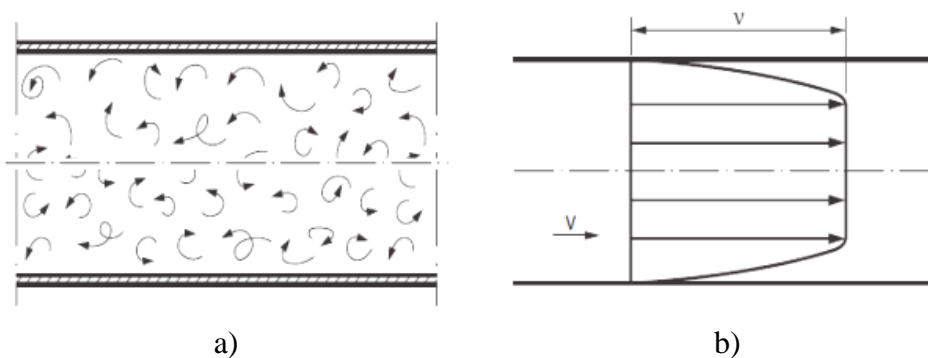


Fig. 2.2. Turbulent flow: a) stream lines; b) velocity profile

The velocity profile for a turbulent flow between two walls is shown in Figure 2.2b. In a turbulent regime, the speed of the particles in each given place constantly changes in a random manner - the flow is unsteady. Vigorous mixing of individual layers of liquid occurs.

2.2 Turbulence models

In this work, one of the main tasks is determining the external forces acting on a body in a fluid flow. The laminar flow behavior is quite simple and well studied, which cannot be said to the same extent about turbulent flow. In addition, turbulent flow is more common in industrial or aerodynamic applications. Due to the enormous influence of the effect of turbulence on the results of the calculations, the use of a suitable turbulence model from the point of view of the formulation of the problem is a critical aspect of the work.

At the moment, there is a whole set of different types of turbulence models, varying in complexity, suitability for a particular task, and the required computational resources.

The most know turbulence models at this time are:

- Direct Numerical Simulation (DNS);
- Large Eddy Simulation (LES);
- Detached Eddy Simulation (DES).
- Reynolds-Averaged Navier-Stokes equations (RANS);
 - Spalart–Allmaras turbulence model (SPA);
 - k - ε model;
 - k - ω model;
 - k - ω SST model;

Figure 2.3 shows a schematic comparison of these models based on the required computational costs and the number of computed parameters versus simulated ones.

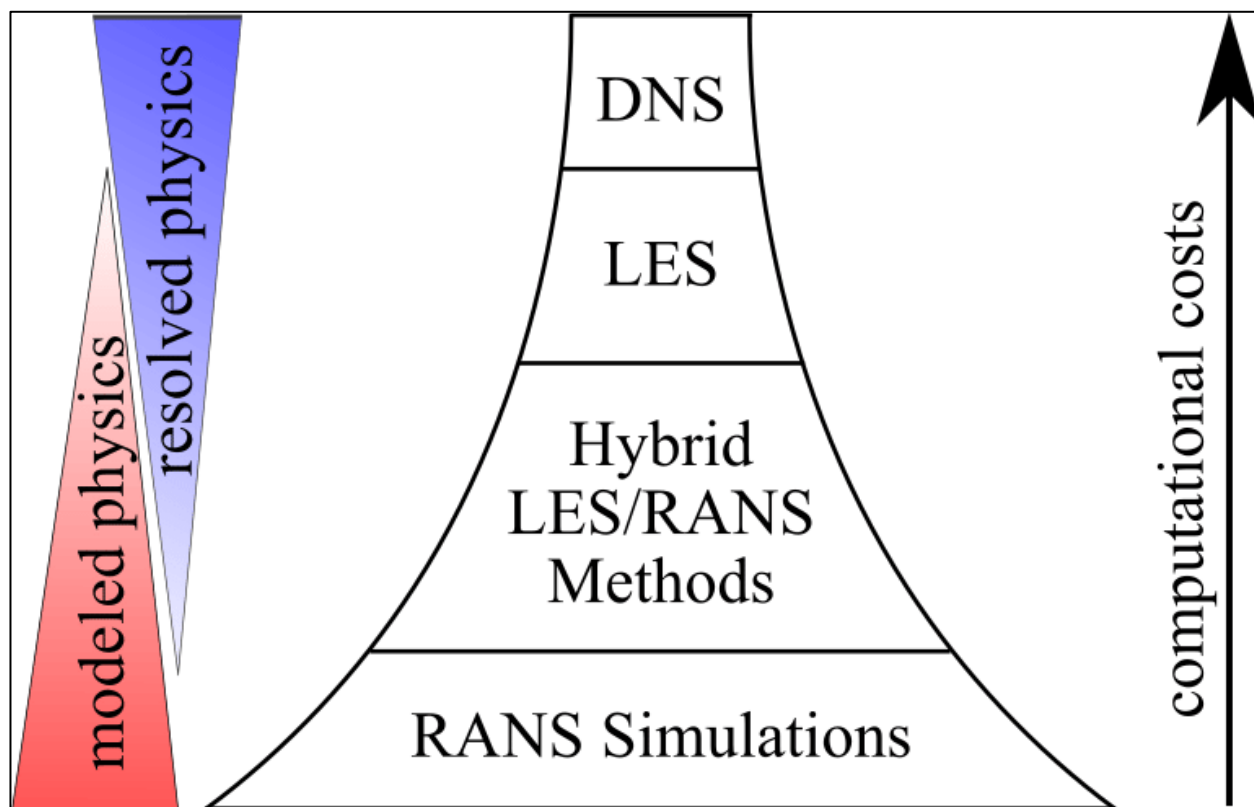


Fig. 2.3. Schematic comparison of turbulence models (Heng X., Paola C. 2019)

As can be seen from the comparison, the models based on the Reynolds-averaged Navier-Stokes equations have the least computational power requirements of the equipment used.

Since the nature of the behavior of the flow in the vicinity of the wall has a dominant effect on the accuracy of calculations of forces, it is worth giving an idea of what processes occur in the near-wall zone.

2.2.1 Near-wall layer

In the near-wall zone, the object is a thin layer of fluid in contact with the surface, or as they say, the near-wall (boundary) layer. In the case of seawater flowing around a cylinder, this is a layer of seawater that directly interacts with the outer wall of the cylinder. Within the thickness of the near-wall layer, the flow rate varies from zero to the free flow rate. To explain the behavior of the flow, consider a uniform flow along the surface of a flat plate (Fig. 2.4).

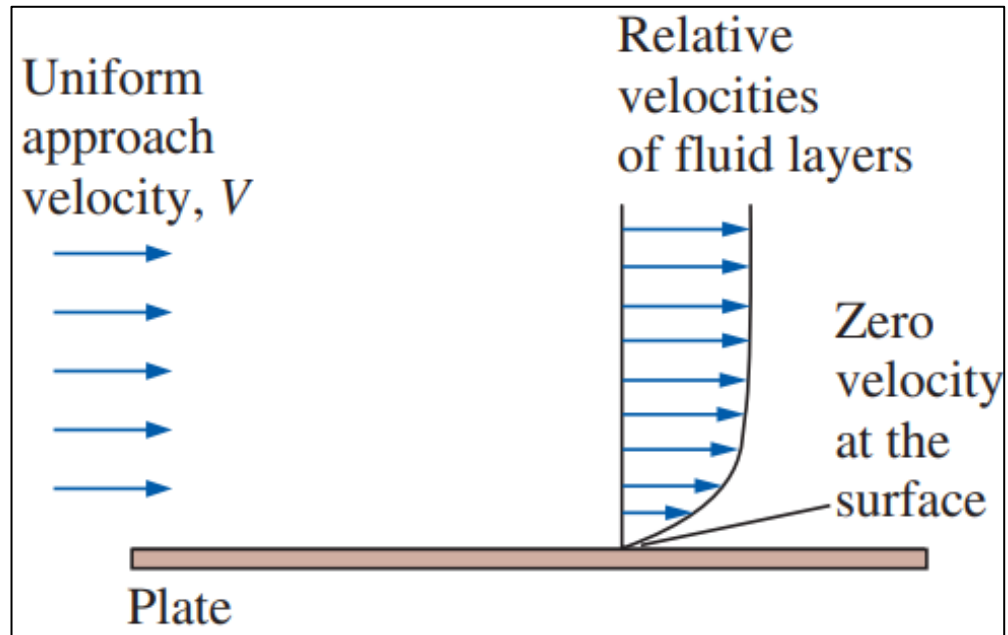


Fig. 2.4. Uniform flow along the surface of a flat plate (Çengel Y. A. and Cimbala J. M., 2010)

It has been observed from experiments that when a liquid flows over a surface, regardless of whether the flow is laminar or turbulent, the liquid particles adjacent to the solid surface will adhere to it. And their speed directly at the contact with a solid surface will be equal to zero. This flow behavior is called the no-slip condition. (Çengel Y. A. and Cimbala J. M., 2010).

Particles slowed down at the boundary with the wall, in turn, affect more distant particles in the flow due to the influence of viscosity and friction between the layers.

Due to the friction of one layer of fluid with an adjacent layer moving at a higher speed, a velocity gradient will appear in the direction perpendicular to the flow, as shown in Figure 4.4.

The flow layer where the velocity gradient is formed and the influence of viscosity and friction is the most significant character called the near-wall layer.

2.2.1.1 Laminar boundary layer

The change in velocity with distance from the wall surface in the near-wall layer under the condition of laminar flow occurs smoothly and can be said evenly, which is shown in Figure 2.5.

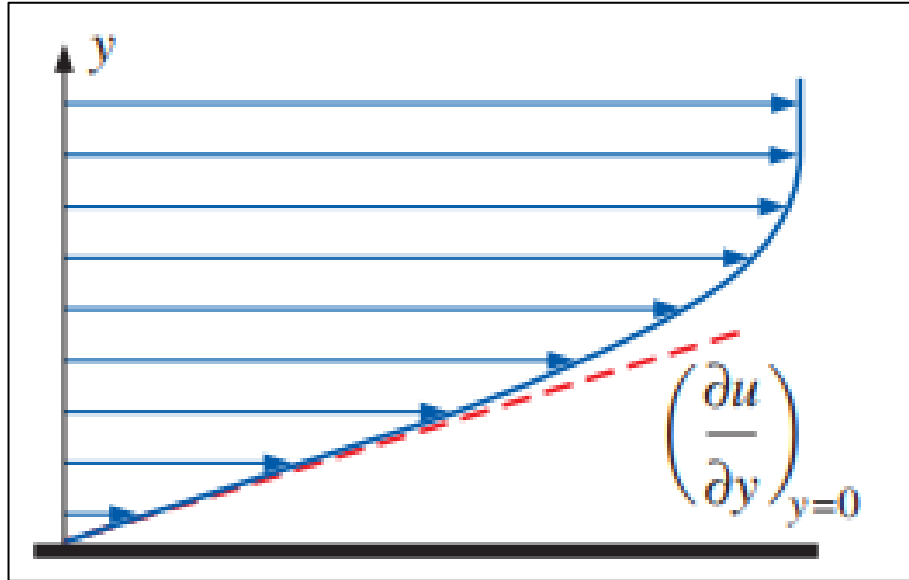


Fig. 2.5. Laminar flow velocity profile (Çengel Y. A. and Cimbala J. M., 2010)

The concept of shear (tangential) stress (τ) was introduced to describe the effect of friction between layers which, according to Newton's law of viscosity (internal friction) for a laminar flow regime, is defined as the product of the viscosity characteristic and the velocity gradient in the direction normal to the surface.:

$$\tau = -\mu \frac{\partial u}{\partial n}, \quad (2.1)$$

where: μ – dynamic viscosity, sP;

u – velocity, m/s.

It is obvious from expression (2.1) that the shear stress is associated with the slope of the velocity profile on the wall surface. The minus sign is due to the dependence on the sign of the velocity gradient to ensure a positive sign of the shear forces.

$$F_{\tau} = A\tau, \quad (2.2)$$

where: F_{τ} – shear force, N;

A – contact area, m².

The Navier-Stokes equations for laminar flow in the near-wall layer under the assumption of an incompressible medium, unsteady flow and disregarding volumetric forces are as follows (Schetz, J. A., & Bowersox):

$$\frac{\partial u}{\partial x} + \frac{\partial v}{\partial y} = 0, \quad (2.3)$$

$$\frac{\partial u}{\partial t} + u \frac{\partial u}{\partial x} + v \frac{\partial u}{\partial y} = -\frac{1}{\rho} \frac{\partial p}{\partial x} + \nu \frac{\partial^2 u}{\partial y^2}, \quad (2.4)$$

where: u – horizontal component of velocity, m/s;

v – vertical component of velocity, m/s;

ρ – medium density, kg/m³;

p – pressure, Pa.

It is also worth noting that for these equations, an assumption was made about a zero pressure gradient in the direction perpendicular to the flow.

2.2.1.2 Turbulent boundary layer

Since in a turbulent regime, in contrast to a laminar one, only the average flow velocity remains constant, while the real velocity fluctuates continuously, the approach described earlier cannot be used for a turbulent flow. The shear stress values are found to be incorrect in comparison with experiments. (Çengel Y. A. and Cimbala J. M., 2010).

Therefore, it was assumed that the real velocity in a turbulent regime could be represented by two components: the mean value and the fluctuating one. In this case, the same decomposition into components can represent the values of the velocity in other directions, as well as the values of pressure (Çengel Y. A. and Cimbala J. M., 2010).

Decomposition values are defined as:

$$u_i = \bar{u}_i + u'_i \quad (2.5)$$

$$p = \bar{p} + p' \quad (2.6)$$

where: u and p represent the values of instantaneous, \bar{u} and \bar{p} , mean, u' and p' fluctuating velocities and pressures respectively.

Since the shear stresses depend on the velocity, the decomposition into components can also be applied to the value of the current shear stress for a turbulent flow. In this case, the first, laminar

component, describes the friction between layers in the flow direction. The second, turbulent component, is associated with friction between fluctuating particles and the rest of the flow (Çengel Y. A. and Cimbala J. M., 2010).

With this interpretation, the resulting value of shear stresses is determined by the expression:

$$\tau_{total} = \tau_{lam} + \tau_{turb}, \quad (2.7)$$

Thus, a new concept is introduced - turbulent shear stress or Reynolds stress, which characterizes the stresses arising due to the formation of turbulent vortices:

$$\tau_{turb} = -\rho \overline{u_i u_j} \quad (2.8)$$

where: ρ – fluid density, kg/m³;

$\overline{u_i u_j}$ – time averaged product of fluctuating components, m²/s²;

In accordance with the assumption of Joseph Boussinesq that in a turbulent flow, the transfer of momentum by vortex formations is similar to molecular diffusion of momentum, since the motion of particles in a vortex is disordered, and when they collide with each other, they transfer momentum, the Reynolds stresses can be written in the following form (Çengel YA and Cimbala JM, 2010):

$$\tau_{turb} = -\rho \overline{u_i u_j} = \mu_t \frac{\partial \bar{u}}{\partial n} \quad (2.9)$$

where: μ_t – turbulent viscosity, sP.

Thus, the total shear stress for a turbulent flow is written as:

$$\tau_{total} = \mu \frac{\partial \bar{u}}{\partial n} + \mu_t \frac{\partial \bar{u}}{\partial n} = (\mu + \mu_t) \frac{\partial \bar{u}}{\partial n}, \quad (2.10)$$

An important aspect is that the behavior of turbulent vortices in free flow and at the boundary with the wall is significantly different. Due to the absence of slippage at the contact with the wall, the formation of flow vortices occurs with low intensity. Therefore, the velocity profile for the turbulent regime (Fig. 2.6) will be significantly different comparing to the laminar velocity profile.

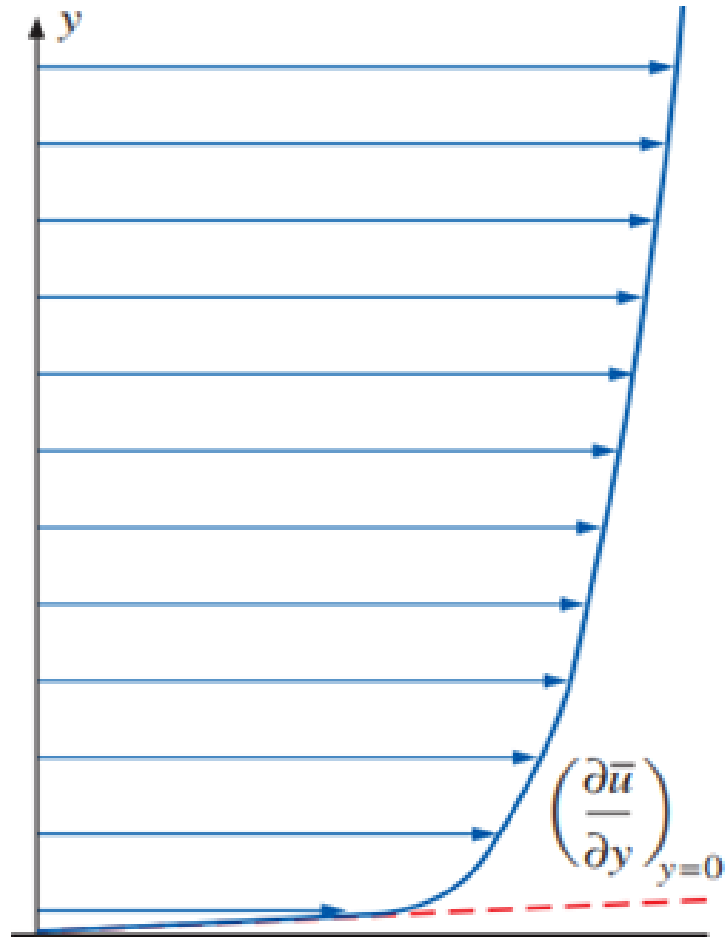


Fig. 2.6. Turbulent flow velocity profile (Çengel Y. A. and Cimbala J. M., 2010)

For a turbulent regime, the velocity far from the wall changes very little, and when approaching the wall, it drops sharply to zero, which leads to an increase in the slope of the tangent and, consequently, to high values of the gradient.

Since the shear stress is directly proportional to the velocity gradient, it can be concluded that for the turbulent regime, the magnitude of the shear stresses will be much higher, comparing with the laminar regime.

2.2.1.3 The law of the wall

For a more detailed description of the flow behavior and velocity change in a turbulent flow close to the boundary with the wall, four main zones can be distinguished (Çengel Y. A. and Cimbala J. M., 2010):

- Viscous sublayer;
- Transition area;
- Logarithmic area;
- Outer zone.

As mentioned earlier, the most important area in modelling the forces acting on a streamlined body is the area near the cylinder wall. It means that it is necessary to describe the layer closest to the wall accurately. Such a layer is a viscous sublayer. Usually, it is very thin, and since it is in contact with the wall, the turbulent effects in it are extremely small, and a laminar component characterizes the shear stress at the wall.

Experiments have shown that a sharp increase in velocity in a viscous sublayer follows an almost linear law (Çengel Y. A. and Cimbala J. M., 2010), where the velocity gradient is represented by the ratio of the velocity to the coordinate perpendicular to the wall:

$$\tau_w = \tau_{total} = \mu \frac{\partial u}{\partial y} = \mu \frac{u}{y} = \rho v \frac{u}{y}, \quad (2.11)$$

where: u – time-averaged flow velocity, m/s.

v – kinematic viscosity, Pa*s.

From where we get the relation:

$$\frac{\tau_w}{\rho} = \frac{uv}{y}, \quad (2.12)$$

Then, introducing the concept of shear stress velocity ($u_* = \sqrt{\tau_w/\rho}$) and substituting it into relation (2.12), we obtain a dimensionless description of the velocity profile for a viscous sublayer:

$$\frac{u}{u_*} = \frac{yu_*}{v}, \quad (2.13)$$

Equation (2.13) is called the law of the wall zone or simply the law of the wall. Based on equation (2.13), we can derive expressions for calculating the thickness of the viscous sublayer (δ_{vs}):

$$y = \delta_{vs} = \frac{5v}{u_*}, \quad (2.14)$$

Introducing dimensionless values:

$$y^+ = \frac{yu_*}{v}, \quad (2.15)$$

$$u^+ = \frac{u}{u_*}, \quad (2.16)$$

It comes to the normalized form of the wall law:

$$y^+ = u^+, \quad (2.17)$$

Figure 2.7 gives a graphical representation of this law and shows a complete picture of the boundary layer and four zones distinguished in the near-wall zone.

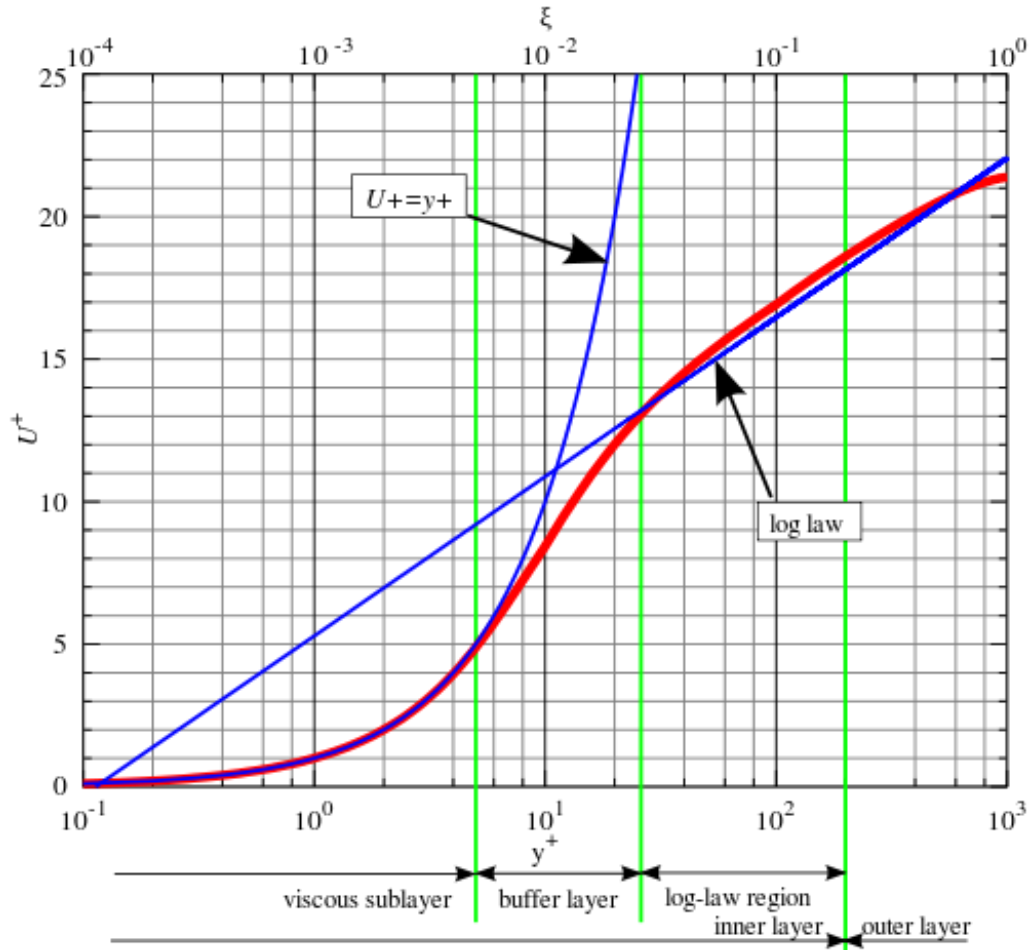


Fig. 2.7. Law of the wall in the turbulent boundary layer.

It was also experimentally found that in the so-called logarithmic zone, the dependence of the velocity on the distance to the wall on a logarithmic scale falls on a straight line. It means that the change in speed occurs according to the logarithmic law, which is where the name of this zone comes from:

$$u^+ = \frac{1}{k} \ln(y^+) + B, \quad (2.18)$$

where: k – Karman constant ($k=0.4$);

B – empirical constant ($B=5$).

Different models of turbulence have their specified requirements for the value of y^+ . Based on this value, the thickness of the first mesh layer (y_1) near the wall is determined:

$$y_1 = \frac{y^+ \nu}{u_*}, \quad (2.19)$$

2.2.2 Direct Numerical Simulation

Direct Numerical Simulation (DNS) is a simulation in which the Navier-Stokes equation is solved without any turbulence model or time averaging to capture the fastest fluctuations or turbulent flow (Orszag S., 1970).

This method requires an extremely small time step and has enormous memory requirements. Moreover, it is the most expensive in terms of the required computational resources since it performs numerous parallel solutions to complex equations.

2.2.3 Large Eddy Simulation

Large Eddy Simulation (LES) is a numerical method used to simulate turbulent flows, based on the concept that large-scale flow motions are explicitly computed. At the same time, the effects of smaller universal scales are modelled. Finally, the Navier-Stokes equations are spatially filtered to obtain the basic equation of this model.

The LES model is used to capture a large turbulent flow structure away from a wall and flow around a streamlined body or flow at a low Reynolds number (Germano et al., 1991).

However, one of the disadvantages of LES is that a very fine mesh must be used around the body wall. As a result, computational costs increase significantly. Although it has been proven to give good simulation results, it is too expensive and time-consuming, so it has not found widespread use in the industry.

2.2.4 Detached Eddy Simulation

Although dual equation models provide a good tradeoff between complexity and accuracy among RANS models, their application is limited to steady-state flow.

Therefore, to solve some kinds of problems, a new approach is required. That will provide computational efficiency and predict the chaotic nature of flows, such as the separation of vortices. It

results in a hybrid model based on the LES and RANS models known as detached eddy simulation (DES). DES combines the best aspects of RANS and LES into a single solution strategy (Spalart, 2009)

In this method, the model switches to formulating a subgrid-scale in areas small enough for LES calculations. Network generation is more difficult than for the simple RANS or LES case due to the RANS-LES switch. (Fröhlich J, von Terzi D., 2008)

DES is computationally expensive compared to RANS using 3D modelling and is not quite suitable for use in this project due to limited computational resources.

2.2.5 Reynolds-Averaged Navier-Stokes equations

The Reynolds-averaged Navier-Stokes equations are a model based on the time-averaged fluid flow equation of motion. The RANS equations determine the average speed and pressure.

In addition, it is assumed that the flow is independent of time. However, this assumption is incorrect in the case of the turbulent flows, as processes in the wake behind a cylinder are unsteady. Therefore, time-dependent RANS formulations are needed to describe such a flow.

The URANS unsteady flow model is known as a very useful mathematical model for solving turbulent flow problems.

Compared to the LES model, the URANS results show the same trends with acceptable accuracy. LES gives better agreement than URANS (Catalano et al, 2003)

In terms of lift, drag forces and Strouhal number, the results obtained by solving the URANS equations allow us to consider them sufficiently effective and suitable for modelling the flow around a cylinder. However, predicting behavior in the boundary layer is still a challenge for URANS. (Catalano et al., 2003)

The URANS equations are a development of the Navier-Stokes equations of motion for an incompressible Newtonian fluid:

$$\frac{\partial u_i}{\partial t} + u_j \frac{\partial u_j}{\partial x_j} = f_i - \frac{\nabla p}{\rho} + \nu \frac{\partial^2 u_i}{\partial x_j \partial x_j}, \quad (2.20)$$

where: ν – kinematic viscosity;

f_i - vector representing external forces.

The concept behind the equations is the Reynolds decomposition, where the instantaneous value is decomposed into its time-averaged and fluctuating values as described in the chapter (2.2.1.2).

In the Reynolds-averaged approach, almost all of the turbulent flow instabilities are modelled, and the slow changes in the mean flow are solved explicitly.

Substituting the expansion terms (2.5) and (2.6) into the Navier-Stokes equation (2.20), we obtain the equation of the URANS model, which has the following form:

$$\rho \frac{\partial u_i}{\partial t} + \rho \frac{\partial u_i u_j}{\partial x_j} = \rho f_i + \frac{\partial}{\partial x_j} (2\mu \overline{S_{ij}} - \rho \overline{u'_i u'_j}), \quad (2.21)$$

where: $\overline{S_{ij}}$ – mean strain rate tensor:

$$\overline{S_{ij}} = \frac{1}{2} \left(\frac{\partial \overline{u_i}}{\partial x_j} + \frac{\partial \overline{u_j}}{\partial x_i} \right), \quad (2.22)$$

It is necessary to determine the value of the Reynolds stress tensor $\rho \overline{u'_i u'_j}$ to solve the URANS equations for the properties of the mean turbulent flow. It is a symmetric second-order tensor with six independent components. There are four unknown properties of the mean flow for conventional three-dimensional flows, namely three components of velocity and pressure.

Taken together, six independent components of the Reynolds stress tensor and four average flow rates give ten unknowns. The transformation of the mass and the three components of the momentum conservation equation gives only four equations to determine the ten unknowns. Hence, more equations or assumptions are required to solve the problem.

The most widely used assumption used in the URANS model is the Boussinesq eddy viscosity assumption (Schmitt, 2007). It is the basis for all two-equation models and the postulate that the Reynolds stress tensor is proportional to the mean strain rate tensor S_{ij} :

$$\overline{u'_i u'_j} = \tau_{ij} = 2\mu_t S_{ij} - \frac{2}{3} \rho k \delta_{ij}, \quad (2.23)$$

where: μ_t – eddy viscosity;

k – mean kinetic energy of turbulence.

A scalar property called vortex viscosity is usually computed over two velocity variables, and the last term is included to simulate the flow of an incompressible fluid and thus to enforce the definition of the kinetic energy of turbulence, satisfies:

$$k = \frac{\overline{u_i u_j}}{2}, \quad (2.24)$$

Boussinesq's hypothesis is an important application of the two-equation turbulence model. This assumption is a huge oversimplification that allows one to think about the effect of turbulence on average flow in the same way that molecular viscosity affects laminar flow. The assumption also allows scalar turbulence variables such as turbulent energy and dissipation to be introduced and related to other variables such as turbulence intensity and turbulence length scale (Bredberg, 2000).

2.2.5.1 Spalart–Allmaras turbulence model

The Spalart–Allmaras turbulence model (SPA) is a single equation model that provides good predictions for some related aerospace simulations. It solves the transport equation for a viscous-like variable (Karim et al., 2008):

$$\frac{D\tilde{\nu}}{Dt} = G_\nu \left\{ \frac{\partial}{\partial x} \left[(\mu_t + \rho\tilde{\nu}) \frac{\partial \tilde{\nu}}{\partial x_i} \right] + C_{b2}\rho \left(\frac{\partial \tilde{\nu}}{\partial x_i} \right)^2 \right\} - Y_\nu + S_{\tilde{\nu}}, \quad (2.25)$$

where: $\tilde{\nu}$ – turbulent kinematic viscosity;

G_ν – production of turbulent viscosity;

Y_ν – destruction of turbulent viscosity;

$S_{\tilde{\nu}}$ – user-defined source term;

C_{b2}, C_{v1} - constants.

Turbulent kinematic viscosity is determined by the expressions:

$$\mu_t = \rho\tilde{\nu}f_{v1}, \quad (2.26)$$

$$f_{v1} = \frac{(\tilde{\nu}/\nu)^3}{(\tilde{\nu}/\nu)^3 + C_{v1}^3}, \quad (2.27)$$

The model is mainly used for applications with moderate separation, such as supersonic/transonic over-wing flow, but does not agree well with experimental results when compared to other models, such as DNS (Constantinides, Oakley, 2006).

2.2.5.2 k-ε model

The k-ε model is a two-equation model in which the transport equations are solved through turbulent kinematic energy (k) and its rate of dissipation (ε) (Wilcox D.C., 2006).

The transport equations for k and ε have the form:

$$\frac{D}{Dt}(\rho k) = \frac{\partial}{\partial x_j} \left[\left(\mu + \frac{\mu_t}{\sigma_k} \right) \frac{\partial k}{\partial x_j} \right] + G_k - \rho \varepsilon, \quad (2.28)$$

$$\frac{D}{Dt}(\rho \varepsilon) = \frac{\partial}{\partial x_j} \left[\left(\mu + \frac{\mu_t}{\sigma_\varepsilon} \right) \frac{\partial \varepsilon}{\partial x_j} \right] + C_{\varepsilon 1} \frac{\varepsilon}{k} G_k - \rho C_{\varepsilon 2} \frac{\varepsilon^2}{k}, \quad (2.29)$$

where: G_k – generation of turbulence kinetic energy;

$C_\mu, C_{\varepsilon 1}, C_{\varepsilon 2}, \sigma_k, \sigma_\varepsilon$ – constants;

k – turbulence kinetic energy;

ε – rate of dissipation.

The turbulent viscosity in this case is determined by the expression:

$$\mu_t = C_\mu \rho \frac{k^2}{\varepsilon}, \quad (2.30)$$

In addition, the improved near-wall treatment modifies the values of turbulent viscosity and scattering velocity near the surface of the cylinder to account for the predominant effects of laminar viscosity.

This model is widely used due to its reliability, computational economy, and sufficient accuracy when simulating the flow around a stationary cylinder.

Near the wall region, k-ε uses an empirical formula known as the wall function to predict flow in order to save computational power. However, while the wall function reduces computational costs, it is insufficient to represent a complex flow accurately.

2.2.5.3 k- ω model

The k- ω model is a two-equation model in which the transport equations are solved in terms of turbulent kinetic energy and specific dissipation rate. In this case, the specific dissipation rate is defined as:

$$\omega = \frac{\varepsilon}{k}, \quad (2.31)$$

The kinetic energy of turbulence and the specific dissipation rate are determined from the following transport equations:

$$\frac{\partial}{\partial t}(\rho k) + \frac{\partial}{\partial x_i}(\rho k u_i) = \frac{\partial}{\partial x_j} \left(\tau_k \frac{\partial k}{\partial x_j} \right) + G_k - Y_k + S_k, \quad (2.32)$$

$$\frac{\partial}{\partial t}(\rho \omega) + \frac{\partial}{\partial x_i}(\rho \omega u_i) = \frac{\partial}{\partial x_j} \left(\tau_\omega \frac{\partial \omega}{\partial x_j} \right) + G_\omega - Y_\omega + S_\omega, \quad (2.33)$$

where: G_k – generation of turbulence kinetic energy;

G_ω – generation of dissipation;

S_k and S_ω – user-defined source terms;

Y_k, Y_ω – dissipation of k and ω due to turbulence;

τ_k, τ_ω – effective diffusivity k and ω .

The coefficients of effective diffusion of energy and dissipation are calculated using the expressions:

$$\tau_k = \mu + \frac{\mu_t}{\sigma_k}, \quad (2.34)$$

$$\tau_\omega = \mu + \frac{\mu_t}{\sigma_\omega}, \quad (2.35)$$

where: μ_t – turbulent viscosity;

σ_k, σ_ω – turbulent Prandtl numbers.

The wall layer depends on the nature of the flow. Therefore a fine mesh is required near the wall. The k- ω model allows for a better description of the flow against a wall. However, one of the disadvantages of this model is its sensitivity to free flow values.

2.2.5.4 k- ω SST model

The SST k- ω model is another two-equation model developed by Menter (1994). It combines the reliability and accuracy of the near-wall k- ω model with the k- ϵ model, which is independent of the far-field incident flow. To do so, the k- ϵ model is converted to a k- ω model.

For the SST k- ω model, the transport equations have the same form as the standard model, except for the added cross-diffusion coefficient. The full form of the equations is as follows:

$$\frac{\partial}{\partial t}(\rho k) + \frac{\partial}{\partial x_i}(\rho k u_i) = \frac{\partial}{\partial x_j} \left(\tau_k \frac{\partial k}{\partial x_j} \right) + G_k - Y_k + S_k, \quad (2.36)$$

$$\frac{\partial}{\partial t}(\rho \omega) + \frac{\partial}{\partial x_i}(\rho \omega u_i) = \frac{\partial}{\partial x_j} \left(\tau_\omega \frac{\partial \omega}{\partial x_j} \right) + G_\omega - Y_\omega + D_\omega + S_\omega, \quad (2.37)$$

The cross-diffusion coefficient is determined using the expression:

$$D_\omega = 2(1 - F_1)\rho\sigma_\omega k \frac{\partial k}{\partial x_j} \frac{\partial \omega}{\partial x_j}, \quad (2.38)$$

where: F_1 – a blending functions that softens the transition of a solution between two models/

The model considers the transfer of turbulent shear stress within the boundary layers by modifying the turbulent eddy viscosity function. The goal is to improve the forecasting accuracy of flows with strong negative pressure gradients and flows with pressure-induced separation of the boundary layer. (Menter, 1994)

Chapter 3

3 Vortices and Vibrations

In this work, the main physical phenomenon important for the correct solution of the problem is the vibrations of the riser. Vibrations come from the action of forces caused by the formation of vortices in the flow behind it. Therefore, it needs to describe general aspects playing a major role in this process. This chapter gives a view on vortex, a description of the mechanism of their formation behind the cylinder and the causes of vibrations.

3.1 Vortex (Eddy) Definition

It is first necessary to explain the vortices themselves to begin the study of the vortex formation mechanism. In general terms, a vortex or eddy is an area in which the flow rotates around an axis. A vortex often forms around low-pressure areas and attracts fluid to its center, creating a spiral-shaped area (Fig. 3.1).

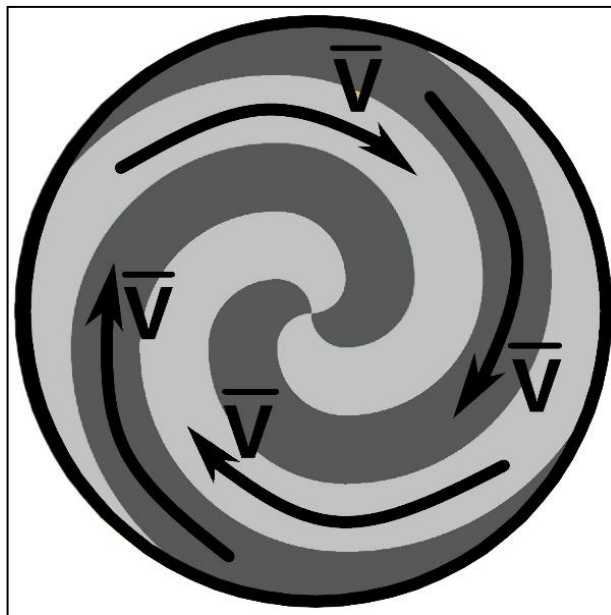


Fig. 3.1. Schematic view on the vortex

Eddies are the main component of a turbulent flow. The following parameters are used to characterize vortices:

- Speed distribution;
- Vorticity;
- Circulation concept

3.2 Vortex Shedding Mechanism

Let's say we have a motionless cylindrical body. When the flow approaches this body, the flow slows down as it interacts with the boundary of the cylinder. The pressure on this side increases. The flow has two paths: up and down around the cylinder. It results in friction against the wall, creating a boundary layer (Fig. 3.2).

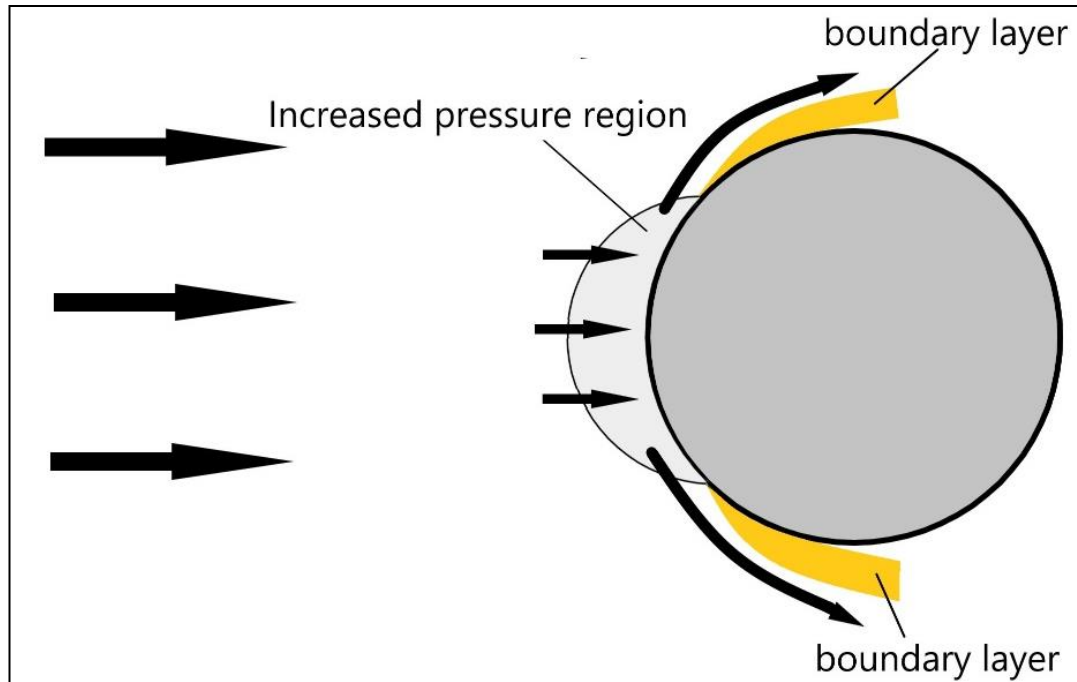


Fig. 3.2. Flow structure at the boundary surface

As the pressure on the face of the cylinder increases, the pressure at the top and bottom will be relatively less. It leads to an increase in the speed of fluid around the body. However, the convection of the liquid behind the cylinder creates a rotation. The rotational speed is less than straight motion. Thus, the fluid velocity decreases again, and therefore the pressure is restored. Such a high-low-high pressure system (Fig. 3.3) creates conditions where the fluid after the cylinder is repelled due to the pressure gradient.

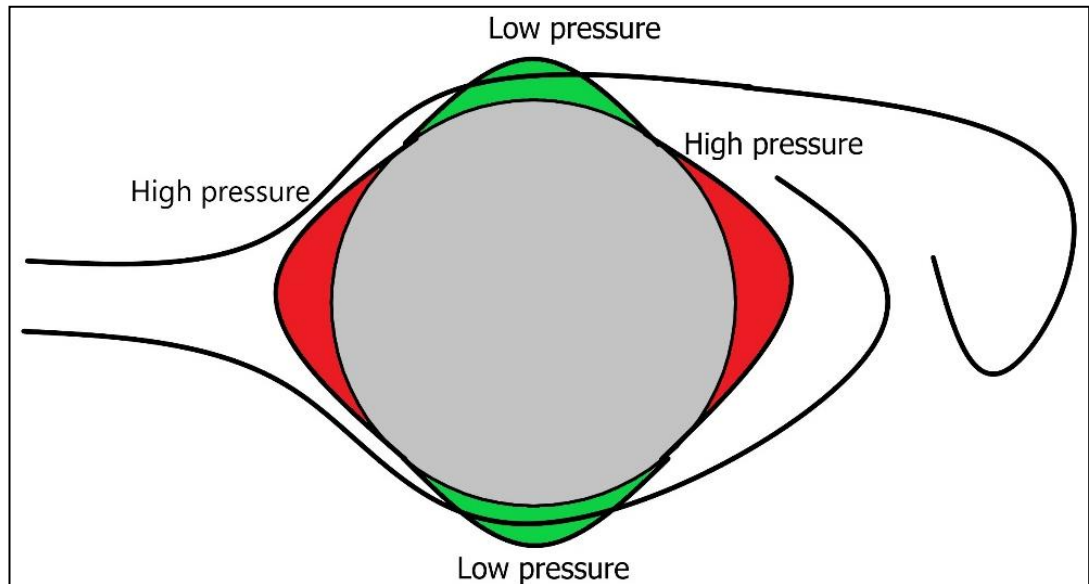


Fig. 3.3. Pressure system around the fixed cylinder

It can be seen from this system that there are two pressure gradients. One acts on the flow before it has circled the cylinder, causing the fluid to accelerate, while the other acts behind the cylinder to push the fluid back into the low-pressure areas.

For these two opposite flows, there is a point where the pressure gradient is neutral. If there is no more pressure gradient, the speed does not change.

From the formula of the shear stress for Newtonian fluids:

$$\tau = \mu \frac{dU}{dy}, \quad (3.1)$$

where: U – flow velocity, m/s;

μ – dynamic viscosity, m²/s.

it is obvious that if the velocity is constant, then there is no shear stress in the fluid at the boundary.

The point under discussion corresponds to the separation point and is illustrated in Figure 3.4. Particles of liquid are separated from the cylinder, forming a shear layer in which there is a significant velocity gradient. Due to the velocity gradient in the shear layer, rotational motion is created in the flow (Muk C.O., 2020).

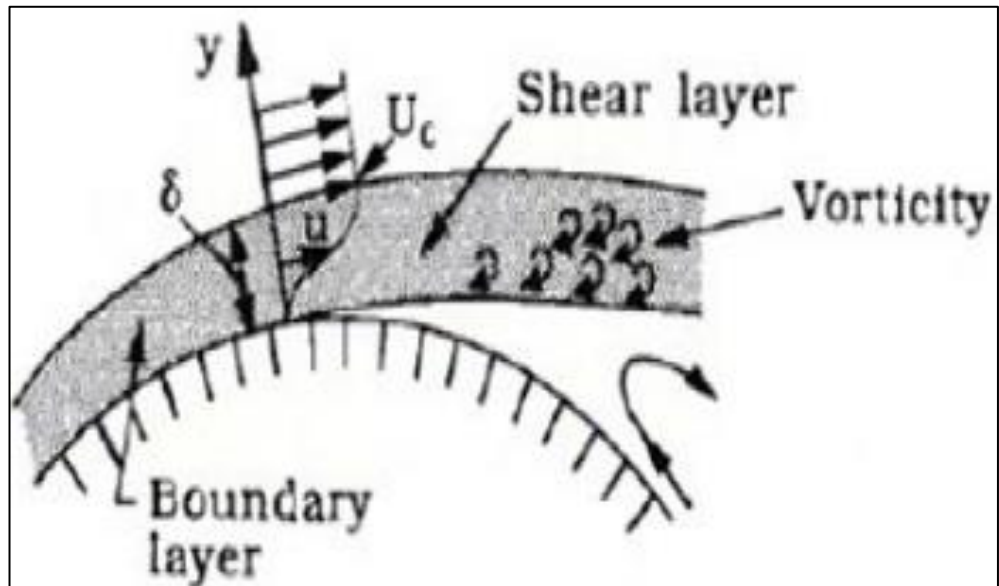


Fig. 3.4. Detailed picture of flow near to separate (Sumer B., Fredsoe J., 2006)

From the upper edge of the cylinder, the rotation of the vortices is clockwise, and at the bottom, counterclockwise. These two oppositely directed rotational fluids then cut off each other to form vortices (Fig. 3.5). Thus, vortices are first formed on one side of the cylinder and then sheared off on the other side.

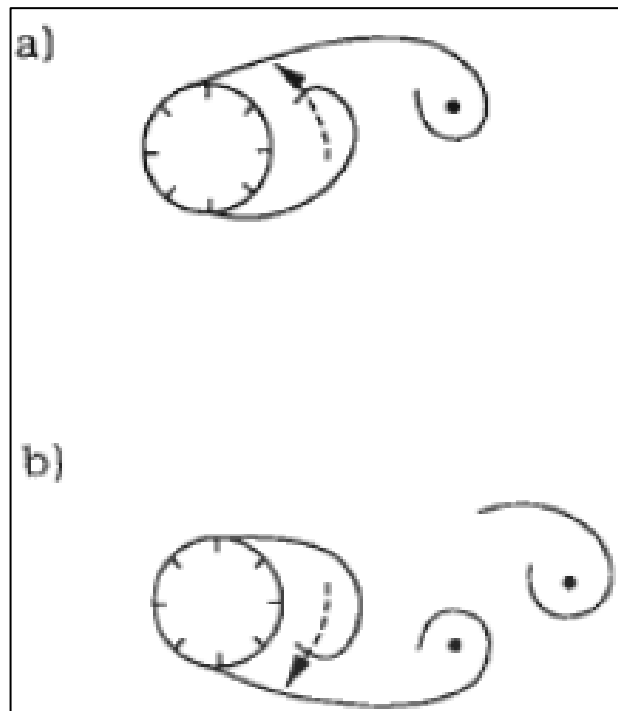


Fig. 3.5. Vortex forming (Sumer B., Fredsoe J., 2006)

This process is periodically repeated, and the frequency corresponding to this period is called the frequency of vortex formation.

3.3 Vortex Shedding After Fixed Cylinder

Vortex shedding is an oscillating flow that occurs when a moving fluid hits an obstacle. Vortices periodically form on one side, and the other side of the obstacle after the flow has passed it. A sequence of such vortices is also known as the von Karman vortex street. This phenomenon depends on the flow rate, shape and size of the body.

The most fundamental body shape for solving the problem of vortex formation is a circular cylinder (Fig. 3.6). It corresponds to the problem of flow around a pipeline or riser.



Fig. 3.6. Vortex shedding after the cylindrical body

Problems of this type have been widely studied because of their relevance for many important practical applications such as marine design, wind load on high-rise buildings, etc.

However, even in the case of simple cylindrical geometry, the flow has a rigid structure, and its behavior differs significantly depending on the Reynolds number.

The flow structure behind a cylindrical body can be described by a combination of three important zones:

- Boundary layer
- Shear layer
- Wake

Since the flow behavior is highly dependent on the Reynolds number, the flow can be divided into different stages. According to a study (Sumer M., Fredsøe's J., 2006), the flow structure and Reynolds number represent the following relationships:

1. No separation ($Re < 5$):



2. A fixed pair of symmetric vortices ($5 < Re < 40$):



3. Laminar vortex street ($40 < Re < 200$):



4. Below subcritical region ($200 < Re < 300$):



Transition to the turbulence in the wake.

5. Subcritical region ($300 < Re < 3 \times 10^5$):



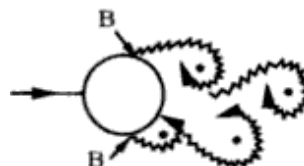
Wake completely turbulent. Laminar boundary layer separation at A.

6. Critical (Lower transition) region ($3 \times 10^5 < Re < 3.5 \times 10^5$):



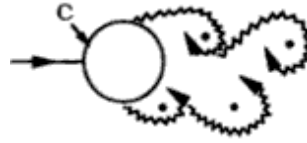
Laminar boundary separation at A. Turbulent boundary layer separation at B, but boundary layer laminar.

7. Supercritical region ($3.5 \times 10^5 < Re < 1.5 \times 10^6$):



Turbulent boundary layer separation at B. Boundary layer partly laminar partly turbulent.

8. Upper transition region ($1.5 \times 10^6 < Re < 4 \times 10^6$):



Boundary layer completely turbulent at one side.

9. Transcritical region ($4 \times 10^6 < Re$):



Boundary layer completely turbulent at both sides.

3.4 Vortex-Induced Vibrations

The previous chapter is devoted to the stationary cylinder. If we talk about real pipelines and risers, then, in fact, not all of their parts are fixed. In this case, the body moves due to pressure gradients, the influence of flow and the formation of vortices.

3.4.1 VIV Principle

Consider a flow U going from left to right and not a fixed cylindrical body. As stated earlier, there is a high-low-high pressure system. However, the flow will now create forces that move the cylinder.

Oscillatory forces will be directed mainly perpendicular to the flow. It usually called a transverse force and cross-flow vibration. The smaller component of the force will act in the direction of the current, so called in-line force and vibration. The frequency of this in-line force is usually twice that of the cross-flow force. (Lie H., Kaasen K.E, 2006)

A graphic representation of the trajectories of the cylinder displacement under the action of these forces for the case under consideration is shown in Figure 3.7.

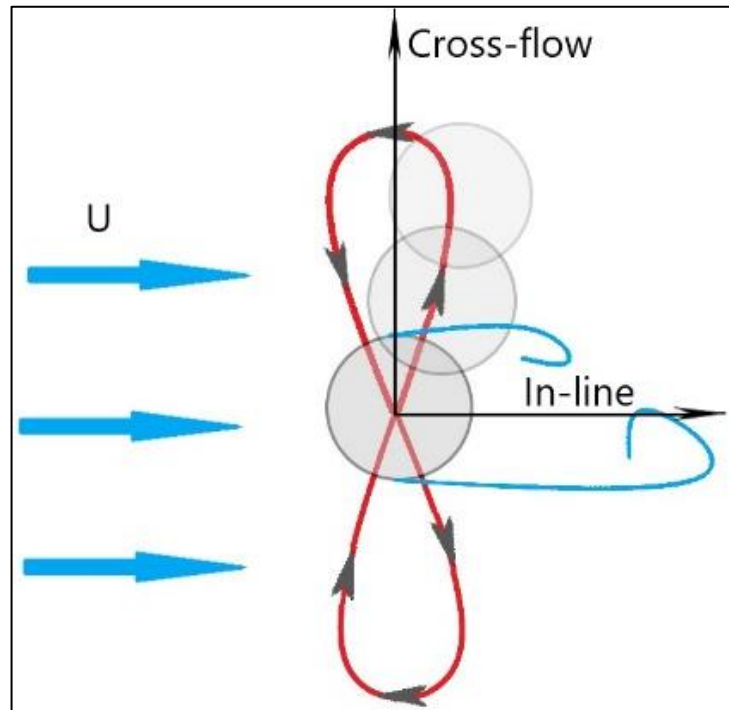


Fig. 3.7. Cylinder vibration principle

Both in-line and cross-flow movement of the cylinder will be periodic. This vibrational movement of the body is repeated in the presence of flow. Therefore it is called vibration.

Vibrations are generated by two forces: drag force (F_D) and lift force (F_L). The average values of these forces are related to the corresponding coefficients:

$$C_D = \frac{\overline{F_D}(t)}{0.5\rho U^2 D}, \quad (3.2)$$

$$C_L = \frac{\overline{F_L}(t)}{0.5\rho U^2 D}, \quad (3.3)$$

where: U – free stream velocity, m/s;

D – cylinder diameter, m;

ρ – fluid density, kg/m³.

C_D, C_L – drag and lift coefficient;

$\overline{F_D}, \overline{F_L}$ – drag and lift forces, N.

3.4.2 Key Parameters

The following parameters are used to analyze vortex vibration:

1. Reynolds number;

2. Strouhal number;
3. Vortex shedding frequency;
4. Eigen (natural) frequency;
5. Oscillating frequency;
6. Amplitude to diameter ratio;
7. Reduced velocity;
8. Mass ratio.

3.4.2.1 Reynolds Number

The Reynolds number is the ratio between inertial forces and viscous forces in a fluid. It helps determine which forces will prevail and whether the flow will be turbulent or laminar. Expression for the Reynolds number when considering a cylinder:

$$Re = \frac{UD}{\nu}, \quad (3.4)$$

3.4.2.2 Strouhal Number

The Strouhal number is the ratio of the inertial forces due to the local acceleration of the flow to the inertial forces due to the convective acceleration. It is related to the frequency of vortex formation, and this relationship, for a cylinder, is written by the expression:

$$St = \frac{f_v D}{U}, \quad (3.5)$$

where: f_v – vortex shedding frequency, s^{-1} .

The Strouhal number is associated with the nature of the flow, which is reflected in many literary sources and studies by the dependence of the Strouhal number on the Reynolds number (Achenbach E. and Heinecke E., 1981, Jiang H. and Cheng L, 2017, Kim Ildoo and Wu X. L., 2015). Figure 3.8 shows a graph of this dependence, which also displays the effect of surface roughness.

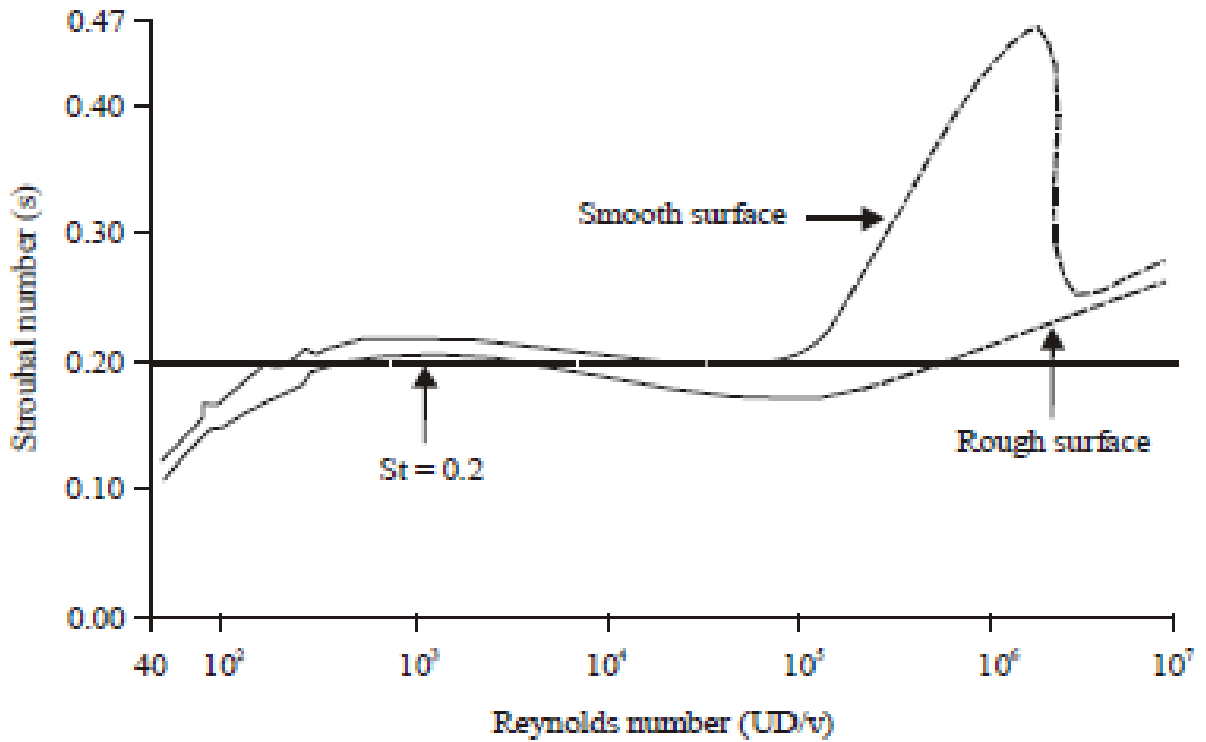


Fig. 3.8. Strouhal-Reynolds number relationship (Zahari M.A., Dol S.S, 2015)

Since most risers and pipelines are subcritical Reynolds numbers, you will find that, according to the relationship between Strouhal numbers and Reynolds numbers, the average St is about 0.2.

3.4.2.3 Frequencies Definition

The natural frequency is the frequency at which the system oscillates when not subjected to a continuous or repetitive external force. It is important because this value is the basic parameter based on which further analysis is carried out.

For a cylinder in vacuum, the natural frequency is defined as (Gabbai R.D., Benaroya H., 2008):

$$f_n^{vac} = \frac{1}{2} \sqrt{\frac{k}{m}}, \quad (3.6)$$

where: k – stiffness, N/m;

m – cylinder mass, kg.

However, if the cylinder is in water, then due to the displacement of a certain mass of water by the cylinder, a pushing force will be created, determined by Archimedes' law. In addition, when the cylinder vibrates in water, it will displace a certain mass of water, which is called the added mass.

The added mass is the mass of seawater that interacts with the pipe during oscillatory movements. It is determined by the mass of displaced water with a coefficient corresponding to the geometry of the object and is calculated as:

$$m_a = \frac{1}{4} C_a \pi \rho_w D^2 L = C_a m_{dw}, \quad (3.7)$$

where: m_a – added mass, kg;

C_a – added mass coefficient;

ρ_w – seawater density, kg/m³;

The change in added mass can be negative or positive, causing the natural frequency to rise or fall. (Lie H., Kaasen K.E, 2006)

Given these facts, the natural frequency of the cylinder is written as (Gabbai R.D., Benaroya H., 2008):

$$f_n^{water} = \frac{1}{2} \sqrt{\frac{k}{m+m_a}}, \quad (3.8)$$

Vortex shedding frequency is the frequency at which vortices are formed when they are detached from the cylinder wall. Mathematically, it is found from expression (3.8) through the speed of the external flow, cylinder diameter and Strouhal number and is determined for a fixed cylinder (Lie H., Kaasen K.E, 2006):

$$f_v(f_s) = \frac{USt}{D}, \quad (3.9)$$

When the cylinder is free to move but with resistance, it will respond to cyclic vortex loading. The amount of movement depends on the force created by vortex generation and the responsiveness of the cylinder, which is determined by its mass, damping coefficient and stiffness. In this case, the reaction of the cylinder to an external influence, namely, caused vibrations, will occur at a frequency called the frequency of forced vibrations or the response (oscillating) frequency (f_{osc}).

3.4.2.4 Lock-In Conditions

The lock-in phenomenon refers to a situation when the natural frequency of the research subject numerically coincides with one of the values of the frequency of external influences. When

considering vibrations caused by vortex formation, the frequency of vortex formation is taken as the frequency of external influences.

Globally, we can say that lock-in conditions are observed when the frequencies of the natural and external oscillations enter into resonance. In this case, the response frequency is fixed at this frequency, leading to increased vibration amplitude to the diameter ratio values (A/D). Mathematically, this condition is expressed as:

$$f_{n,t} = f_v = f_{osc} \quad (3.10)$$

However, the natural and vortex frequencies may not exactly match the expected resonant frequency. As described earlier, the natural frequency value is influenced by the added mass. In addition, vibrations of the cylinder under the action of external forces affect the formation and removal of vortices.

Therefore, if the added mass is taken into account, the response frequency or resonant frequency will be equal to some compromise between the current natural frequency and the current vortex frequency.

When analyzing vortex vibrations, the relationship between the natural frequency of a body and the frequency of vortex formation is critically important.

3.4.2.5 Reduced Velocity

The reduced flow rate is defined as:

$$U_r = \frac{U}{f_n D}, \quad (3.11)$$

where: U – free stream velocity, m/s;

f_n – natural frequency of the body in the medium, s^{-1} ;

D – cylinder diameter, m.

Figure 3.9 shows the dependence of the natural frequency to the frequency of vortex formation ratio and the vibration amplitude to the cylinder diameter ratio on the values of the reduced velocity.

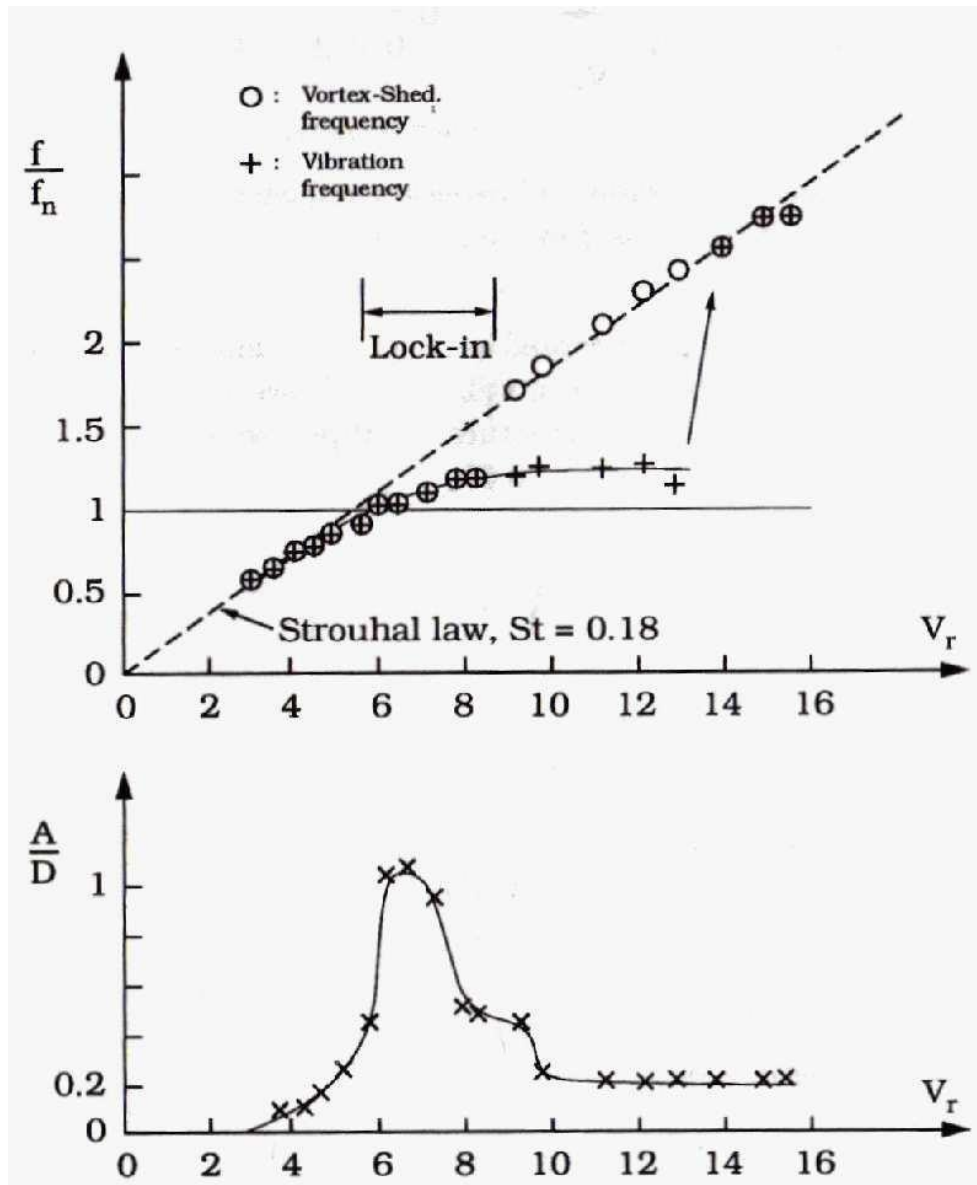


Fig. 3.9. Lock-In conditions at specific reduced velocities (Sumer B., Fredsoe J., 2006)

As can be seen from this graph, the synchronization mode is typical for the range of reduced velocities of approximately [5-10]. Of course, the boundaries of the interval may differ slightly. However, in general, these values of the reduced velocity correspond to many studies and real experiments.

It has been established that the reduced velocities range of lock-in conditions occurrence depends on the ratio of the cylinder mass to the mass of the displaced liquid, called the mass ratio. (Zhao M., Cheng L., 2013, Govardhan, R., Williamson, C., 2000)

3.4.2.6 Mass Ratio

The mass ratio, as mentioned above, is the ratio of the mass of the cylinder to the mass of the water it displaces:

$$m^* = \frac{m}{m_{dw}} = \frac{m}{\rho_w \pi L D^2 / 4}, \quad (3.12)$$

This parameter is used to describe the system's behavior, taking into account the influence of the added mass and buoyancy forces due to the force of Archimedes created by the displaced water.

Chapter 4

4 Oscillating Cylinder Model Description

When solving the problem of oscillation of the cylinder under the action of the forces of the incident flow, it is necessary to consider the resistance forces. These forces prevent displacement and are determined by the stresses arising in the pipe during deformation.

Since the problem is two-dimensional, a widely used approach represents resistance forces by implementing an elastic spring model. The spring virtually supports the cylinder, limiting its movement.

This approach is based on the law of elasticity, in which the forces of resistance to tension or compression are directly proportional to the relative displacement. In this case, the coefficient of proportionality is determined by the properties of the material, namely the stiffness.

$$\Delta F_s = -k\Delta x, \quad (4.1)$$

where: k – spring stiffness, N/m;

Δx –relative displacement, m;

ΔF – resistance forces, N.

In reality, all oscillatory movements are not ideal. Therefore, besides the forces caused by the resistance to displacement, it is necessary to introduce a parameter that describes the intensity of damping when simulating the cylinder oscillations. The corresponding parameter is the damping. It characterizes the intensity of the return of the oscillating object to a static state.

Considering the above, a damped oscillatory system for a cylinder, subject to forces in two directions, will look like shown in Figure 4.1.

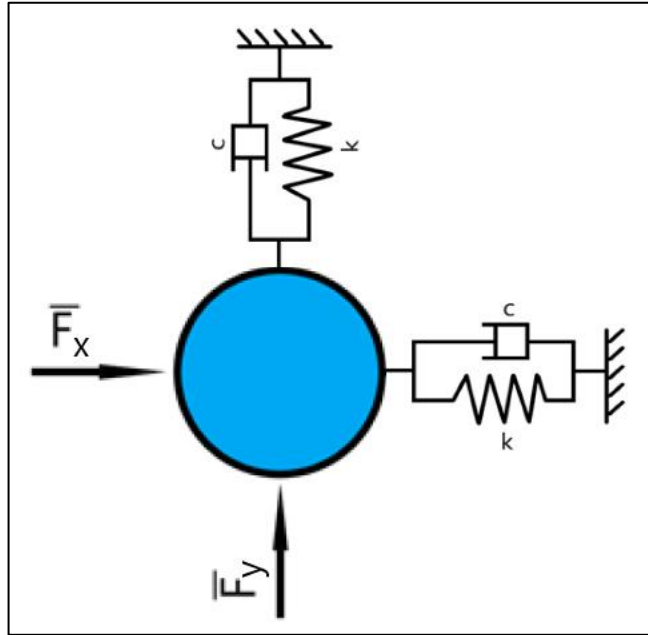


Fig. 4.1. Schematic representation of oscillating cylinder system

The calculation of the displacement amplitudes for the system is based on the equation of motion. The equations of motion for an oscillatory system in two degrees of freedom, taking into account the influence of the added mass, have the form:

$$(\bar{m} + \bar{m}_a)\ddot{x} + c\dot{x} + kx = F_x, \quad (4.2)$$

$$(\bar{m} + \bar{m}_a)\ddot{y} + c\dot{y} + ky = F_y, \quad (4.3)$$

where: \bar{m} – cylinder mass per unit length, kg/m;

\bar{m}_a – added mass per unit length, kg/m;

$\ddot{x}, \dot{x}, x, \ddot{y}, \dot{y}, y$ – acceleration, velocity and displacement of cylinder in x and y directions ;

k – spring stiffness, N/m;

F_x, F_y – external forces in x and y directions, N;

c – damping, m/s.

As far as the riser itself is a hollow cylinder, it is necessary to assume that it is either empty or full when calculating the mass in this problem. With these notes in mind, the mass of the cylinder per unit length is written as:

$$\bar{m} = \frac{1}{4}\pi(D_o^2 - D_i^2)\rho_s + \frac{1}{4}\pi D_i^2 \rho_{fl}, \quad (4.4)$$

where: ρ_s – cylinder material density, kg/m³;

ρ_{fl} – inner fluid density, kg/m³;

D_o, D_i – outer and inner diameters of cylinder, m.

The spring stiffness is determined either by the properties of the material or by calculations based on the known values of the natural frequencies by the formula:

$$k = 2 * f_n^2 (\bar{m} + \bar{m}_a), \quad (4.5)$$

where: f_n – the lowest natural frequency, s⁻¹.

The damping of vibrations depends on many input data, for example, on the magnitude of external forces and the diameter of the pipe. This parameter is difficult to predict and is usually set based on experimental studies when modelling a certain problem or is introduced artificially. However, direct experimentation or finding real-world results suitable to be used in particular work is often an impossible task.

Despite this, in order to perform basic analysis, you can select the value of the attenuation factor based on the expected nature of the attenuation.

The ratio of the current damping coefficient to the critical one is used to describe the behavior of the oscillatory system and is called the relative damping coefficient.

$$\xi = \frac{c}{c_{cr}} = \frac{c}{2\sqrt{k\bar{m}}}, \quad (4.6)$$

where: c – actual damping,

c_{cr} – critical damping.

The expression for the critical damping is derived from the solution of the characteristic equation obtained by transforming the equation of motion. Depending on the nature of the attenuation, the systems are divided into three types:

1. Overdamped ($\zeta > 1$)
2. Critically damped ($\zeta = 1$)
3. Underdamped ($\zeta < 1$)

Figure 4.2 graphically shows the difference between these types of attenuation. The graph shows that types 1 and 2 cannot be called oscillatory. In both cases, the system gradually returns to

equilibrium after a single perturbation. At the same time, for the critical mode, motion stabilization occurs most intensively.

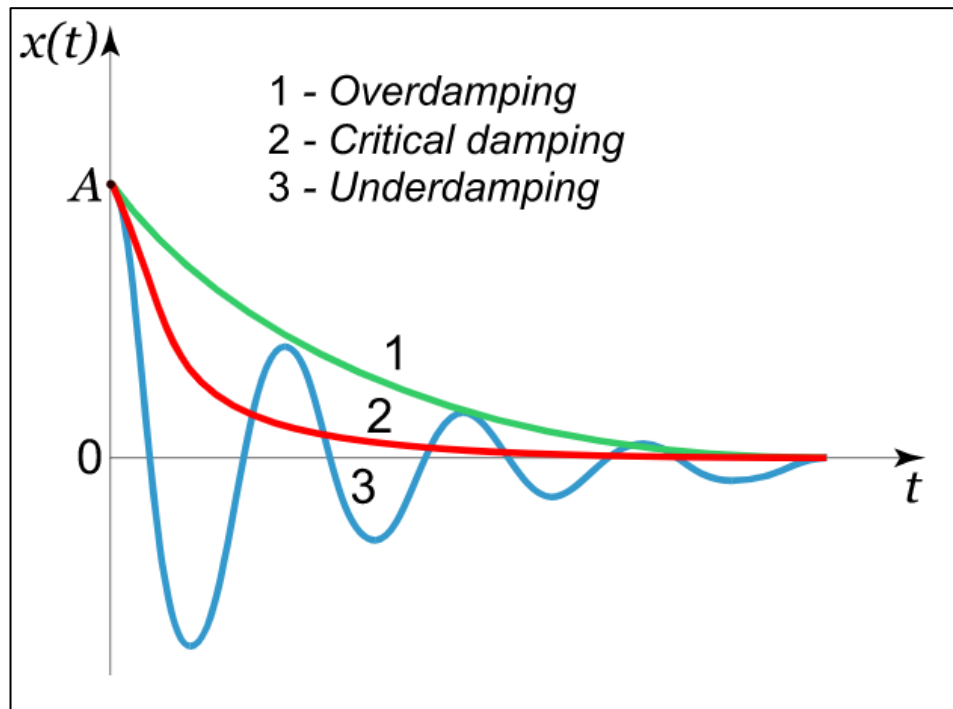


Fig. 4.2. Types of damped oscillations

It can be concluded that for the problem of cylinder oscillation, it becomes necessary to select the 3rd type of damping, and the damping intensity is regulated by the ratio of the current and critical coefficients.

Since this work considers the possible loads on the riser, the most important is the calculation of the system, which is characterized by high-amplitude oscillations. Direct control of the damping coefficient does not make sense since the oscillatory motion will damp only due to the adjusted coefficient. Therefore, a correct approach would be to calculate without taking into account the attenuation, namely, with a zero damping coefficient ($\zeta=0$).

Chapter 5

5 Structural Dynamics

5.1 Modal Analysis

Determining the loads on the elements of the offshore pipeline needs to conduct experimental studies. Depending on the test model, experiments can be divided into flexible pipe tests and rigid cylinder tests. In these tests, bending strain, displacement and acceleration are measured along the pipe. Flexible pipe movements can be reconstructed using modal analysis. Typical vibration tests for coiled tubing are high mode tests (Wu J. et al., 2019).

Modal analysis is the process of determining the internal dynamic characteristics of a system in the form of natural frequencies, damping factors, and vibration modes. It is possible to formulate a mathematical model to get the behavior of a system in dynamics using the results of experiments. The formulated mathematical model is called the modal model of the system (Jimin He, Zhi-Fang Fu, 2001).

Modal analysis is an indispensable tool for understanding the structural dynamics of objects. It allows you to understand how structures and objects vibrate and how resistant they are to applied forces. The modal analysis enables testing and optimization of machines and structures.

The dynamic structural analysis includes frequency and position considerations. It is evidenced by the analytical solution of partial differential equations for continuous systems. In the case of risers, the system is presented as a combination of a beam and a string. Modal analysis is based on the fact that the vibrational response of a linear, time-invariant dynamic system can be expressed as a linear combination of a set of simple harmonic vibrations called natural vibration modes. (Jimin He, Zhi-Fang Fu, 2001)

Natural forms of vibrational displacements of a dynamic system are completely determined by its physical properties (mass, stiffness, degree of damping) and their spatial distribution. Each mode is described in terms of its modal parameters: the natural frequency, modal damping, factor and nature of the displacement, and the mode of vibration are determined. The shape of a mode can be complex, with each mode having its own frequency. The degree of participation of each natural mode in the general vibration process is determined, taking into account the source of excitation and the mode of vibration of the system.

5.1.1 Determination of Natural Frequencies

The stiffness of the flexible pipe model is generally related to the tensile and flexural stiffness. Therefore, the natural frequencies for offshore risers can be found using the combined calculation approach of the natural frequencies for a tensioned string and an untensioned beam. (Wu J. et al., 2019)

In addition, for pipes, depending on the length and characteristics of the material, there are several vibration modes. Its unique harmonic shape distinguishes each mode.

The natural frequencies of a stretched string ($f_{n,s}$) and a beam ($f_{n,b}$) for a certain mode are respectively expressed by the formulas (Wu J. et al., 2019):

$$f_{n,s} = \frac{n}{2} \sqrt{\frac{T}{ML^2}}, \quad (5.1)$$

$$f_{n,b} = \frac{\pi n^2}{2} \sqrt{\frac{EI}{ML^4}}, \quad (5.2)$$

where: n – mode number;

T – averaged tension, N;

M – mass per unit length, kg/m;

L – length, m;

E – Young's modulus, kg/m;

I – area moment of inertia, m⁴.

Combining the above expressions (5.1) and (5.2), we obtain expressions for determining the natural frequency of the riser ($f_{n,t}$):

$$f_{n,t} = \sqrt{f_{n,s}^2 + f_{n,b}^2} = \frac{n}{2L} \sqrt{\frac{T}{M} + \left(\frac{\pi n}{L}\right)^2 \frac{EI}{M}}, \quad (5.3)$$

Calculation of the natural frequencies is necessary for their further comparison with the frequencies of the external influence. The result is the identification of potential modes in which the appearance of the synchronization phenomenon is possible, which is a critically important aspect when studying the behavior of a riser.

5.1.2 Real Response of the Riser

As described earlier, if the natural resonance frequency of the cylinder is not too far from the analytical value of the frequency of the external stimulus, then the phenomenon of synchronization occurs. In this case, vortices are formed at the real vibration frequency but not at the value predicted by the formula. In other words, the movement of the cylinder controls the vortex separation. And the frequency at which oscillatory movements occur is called the frequency of forced oscillations.

It is assumed that the response frequency is a single natural frequency, but since the added mass will vary with frequency and flow rate, a sequence of studies is required for a large number of natural frequencies. The subset of the candidate response frequencies will determine the full set of possible active frequencies. (Lie H., Kaasen K.E, 2006)

In this case, the dimensionless frequency is used for the analysis of potential modes at which lock-in conditions occurs:

$$\hat{f} = \frac{f_{osc}D}{U(z)}, \quad (5.4)$$

where: $U(z)$ – velocity profile along water depth, m/s.

Experimentally was found that the most probable values of the dimensionless frequency at which the synchronization mode is observed refer to the interval [0.125–0.3]. (Muk C.O., 2020)

When the riser is placed in an uneven flow, the change in speed with depth leads to the appearance of a certain interval of natural frequencies, which will coincide with the frequency of the external influence.

It is shown by real tests that both the added mass and the damping intensity depend on the frequency and amplitude. (Lie H., Kaasen K.E, 2006)

The damping intensity increases with an increase in the vibration amplitude, which stimulates the vibrational system to decrease the change in the vibration amplitude, even during lock-in conditions, when it becomes close to one cylinder diameter. Thus, it suggests that the process of vortex vibration is self-limiting.

5.2 Riser Shape Determination

The calculations for defining the riser shape can be based on a multi-strip approach. (Duan et al. 2016, Schulz et al. 2004)

This method is based on selecting a certain number of sections along the length of the riser.

First, the riser is divided into conventional elements along its length, for each of which the mass, damping coefficient, stiffness and external forces are determined.

Further, for each of the sections, the simulation of the flow around the cylinder is performed. The simulation results are the forces that act on the riser in the lateral and longitudinal flow directions at a particular section.

Considering that the displacements of individual elements relative to each other in this case will be small, the flexible cylinder can be modelled as a bending beam with two fixed ends. (Duan et al. 2016, Schulz et al. 2004)

This model is based on the Euler-Bernoulli Beam Theory, or as it is also called the classical beam theory. Then, using the finite element method, it is possible to calculate the cumulative effect of the forces acting on each individual element.

The solving procedure of the dynamic problem is based on representing a riser element using a consistent mass matrix formulation. The resulting equations of motion for each structure is a set of second-order differential equations. (Duan et al. 2016, Schulz et al. 2004)

Thus, the equations of motion for solving such a problem have the form (Duan et al., 2016, Schulz et al., 2004):

$$[m]\ddot{x} + [c]\dot{x} + [k + k_g]x = [F_x], \quad (5.5)$$

$$[m]\ddot{y} + [c]\dot{y} + [k + k_g]y = [F_y], \quad (5.6)$$

where: [m] – elements mass matrix;

[c] – damping matrix;

[k] – stiffness matrix;

[k_g] – geometric stiffness matrix.

It should be noted that the matrices of mass, damping coefficients and stiffness were obtained using the Euler–Bernoulli beam theory for small displacements. Therefore, the matrices consist of four elements of the degree of freedom (two transverse displacements and two angular displacements).

The mass, stiffness and drag coefficient matrices for each element are defined as follows (Duan et al., 2016, Schulz et al., 2004):

$$m_{ij} = \frac{\bar{m}L}{420} \begin{bmatrix} 156 & 22L & 54 & -13L \\ 22L & 4L^2 & 13L & -3L^2 \\ 54 & 13L & 156 & -22L \\ -13L & -3L^2 & -22L & 4L^2 \end{bmatrix}, \quad (5.7)$$

$$k_{ij} = \frac{2EI}{L^3} \begin{bmatrix} 6 & 3L & -6 & 3L \\ 3L & 2L^2 & -3L & L^2 \\ -6 & -3L & 6 & -3L \\ 3L & L^2 & -3L & 2L^2 \end{bmatrix}, \quad (5.8)$$

where: \bar{m} – riser mass per unit length, kg;

E – Young’s modulus, Pa;

I – area moment of inertia, m⁴;

L – element length, m.

The axial tension present in the riser is accounted for by adding the geometric stiffness matrix [k_g] with each element's contribution. This matrix is defined as follows (Duan et al., 2016, Schulz et al., 2004):

$$k_{g_{ij}} = \frac{-T}{30L} \begin{bmatrix} 36 & 3L & -36 & 3L \\ 3L & 4L^2 & -3L & -L^2 \\ -36 & -3L & 36 & -3L \\ 3L & -L^2 & -3L & 4L^2 \end{bmatrix}, \quad (5.9)$$

where: T – local tension of the element, N.

The riser mass per unit length is determined similarly to the problem of modelling cylinder vibrations using the formula (4.4).

The solution of equations (5.5) and (5.6) can be performed using two methods. In the work (Duan et al., 2016), equations are integrated using the Newmark beta method. And in work (Schulz et al, 2004), they used the Runge-Kutta integration scheme of the fourth-order.

5.3 Stresses Calculations

5.3.1 Von Mises Criterion

The von Mises criterion states that if the equivalent stress of a material is equal to or greater than the yield strength of the same material under simple tension, then the material will deform.

Equivalent load is a quantity used to determine whether a given material will deform or fail. Mainly used for ductile materials such as metals.

The expressions for determining the equivalent stress for the riser are (Karunakaran D.N., 2020):

$$\sigma_{eq} = \sqrt{\sigma_h^2 + \sigma_l^2 - \sigma_h \sigma_l}, \quad (5.10)$$

where: σ_{eq} – equivalent stress, Pa;
 σ_h – hoop stress, Pa;
 σ_l – longitudinal stress, Pa.

At the same time, one more component of the original equation is missed - shear stress. In general, the shear stress for the riser is neglected because it is in an upright position. The flow is perpendicular to the pipe and provides zero shear stress.

Tensile stresses are generated in the pipe by pressure. The equilibrium conditions are used (Fig. 5.1) between two pressures (inside the pipe and outside) to determine this stress.

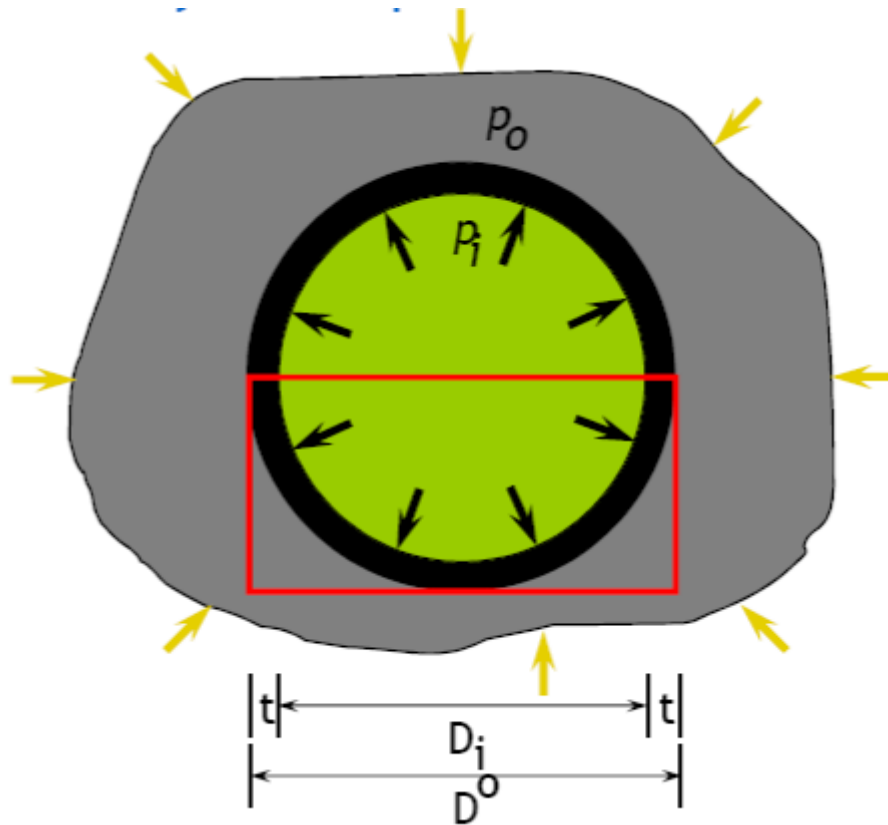


Fig. 5.1. The equilibrium conditions representation (Karunakaran D.N., 2020)

Outside pressure as well as inside pressure cause tension:

$$\sigma_h = \frac{p_i D_i - p_o D_o}{2t}, \quad (5.11)$$

where: t – pipe wall thickness, m;
 p_i, p_o – inner and outer pressure, Pa;

D_i, D_o – pipe inner and outer diameters, m.

It should be noted that even at the stage of pipe design development, it is necessary to carry out calculations for real conditions. This operation is performed to determine the inner and outer radius and wall thickness at which the tensile stress will not exceed the safe design maximum. The maximum is determined based on the yield strength of the selected material.

$$\sigma_h \leq f_1 \sigma_y, \quad (5.12)$$

where: f_1 – design factor (0,6);

σ_y – yield strength, Pa.

Historically, the design factor f_1 was assumed to be 0,72 for pipelines and 0,60 or less for risers (Karunakaran D.N., 2020).

Currently, higher values of the coefficient up to 0.8 and more can be allowed. However, regional regulations and requirements must be observed (Karunakaran D.N., 2020).

Combining equations (5.11) (5.12) and taking into account $2t=(D_o-D_i)$, we obtain expressions for the proper wall thickness.

$$t \geq \frac{(D_i)}{2\left(\frac{(f_1 \sigma_y + p_i)}{(p_i - p_o)} - 1\right)}, \quad (5.13)$$

$$t \geq \frac{(p_i - p_o) D_o}{2(f_1 \sigma_y + p_i)}, \quad (5.14)$$

The outside diameter and design wall thickness are selected based on regulatory standards, and then the inside diameter of the pipe is calculated. This process is repeated until satisfactory relationships between the parameters of a real pipe are found.

A force that causes axial stresses in a section lengthens or shortens it. The effects that can cause axial stress are pressure, temperature and curvature (Fig. 5.2). (Qiang Bai, Yong Bai, 2014)

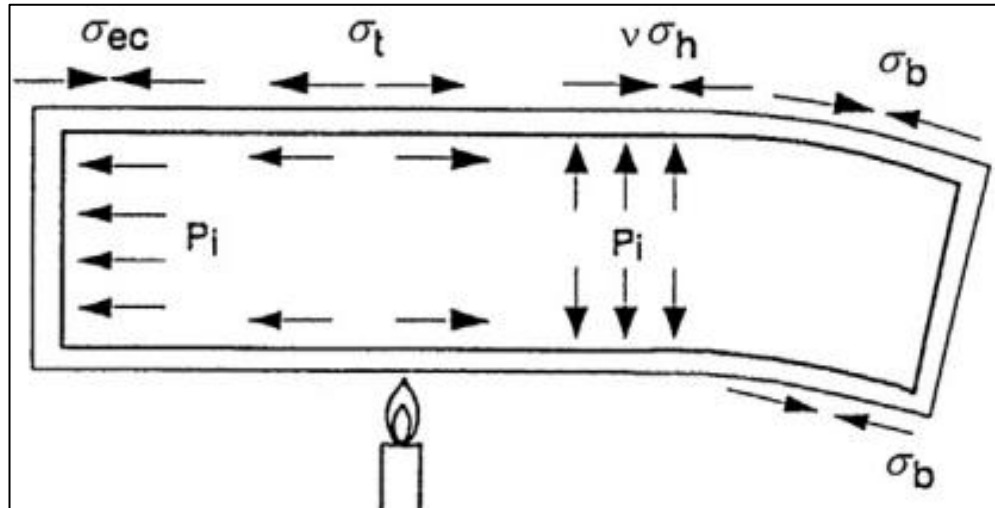


Fig. 5.2. Axial stress decomposition

If the temperature of the pipe increases, it will expand both circumferentially and along the axis. Diametrical expansion is usually completely unrestricted, but longitudinal expansion is constrained by seabed friction and bonding elements.

The longitudinal stress can be calculated using the formula:

$$\sigma_l = \sigma_{ec} + \sigma_t + \nu\sigma_h + \sigma_b, \quad (5.15)$$

where: σ_{ec} – end-cap stress, Pa;

σ_t – thermal stress, Pa;

σ_b – bending stress, Pa;

ν – Poisson ratio (0,3 for steel).

However, a simpler form of calculating the longitudinal stress can be used, which does not consider the stresses at the ends since it does not introduce a noticeable effect and is calculated only in more specific studies.

The calculated value of the equivalent stress is compared with the yield strength, taking into account the design safety factor. f_3 :

$$\sigma_{eq} < f_3\sigma_y, \quad (5.16)$$

The value of this factor is also determined by the regulatory documents, but the typical value is 0.8.

5.3.2 Maximum Bending Stress

When it comes to riser loads, the most significant factor is pipe bending stresses. The tension of the pipe is easier to control compared to its bending under the influence of external influences. With vibration during lock-in conditions, the amplitudes of pipe displacement from the original axis can reach critical values. Bending stresses arise from a bending moment under a transverse load. It is possible to calculate its curvature having equations for determining the shape of the riser along water depth (Larsen C.M. et al., 2006):

$$k(z) = \Phi''(z), \quad (5.17)$$

where: $k(z)$ – pipe curvature;

$\Phi''(z)$ – pipe shape.

By determining the curvature of the riser, we can obtain the minimum radius of curvature for which the greatest deformation will be observed:

$$R_{min} = \frac{1}{k_{max}}, \quad (5.18)$$

Then the maximum relative deformation of the pipe at the place of the minimum radius of curvature is determined by the expression:

$$\varepsilon_{max} = \frac{r_o}{R_{min}} = \frac{D_o}{2R_{min}}, \quad (5.19)$$

where: ε_{max} – relative deformation of pipe;

r_o – pipe outside radius, m.

Knowing the characteristics of the material (including Young's modulus) and the maximum relative deformation, with the help of elastic deformation law, it is possible to calculate the maximum mechanical stress acting in the pipe:

$$\sigma_{max} = \varepsilon_{max}E, \quad (5.20)$$

where σ_{max} – maximum stress, Pa;

E – Young's modulus, Pa.

Chapter 6

6 Modelling and Calculations

6.1 Input data

Since this study is not conducted for a specific field and riser, the conditions of the South Barents Basin, described in Chapter 1.4.2, are used as input data (see Table 6.1) for performing the work. The South Barents Basin has large gas reserves. Therefore, the riser is considered filled with a gas of constant density.

It is assumed that the wellhead is located directly below the platform. Wave loads and the influence of platform movement are not taken into account to simplify further calculations.

Table 6.1. Input data

Water depth	300	m
Seawater dynamic viscosity (T=0°C)	0,00189	Pa*s
Gas density	600	kg/m ³
Seawater density	1025	kg/m ³

6.2 Choosing the riser type

With a water depth of 300 m, the use of steel catenary risers is advisable in case of a large offset of the wellhead relative to the platform. Since it is assumed that the wellhead is not offset from the platform, the most suitable type of riser is a top-tension riser. This type of riser is the easiest to manufacture and install.

Taking into account the seawater flow velocity profile (Figure 1.2), a schematic representation of the research problem can be depicted as in Figure 6.1.

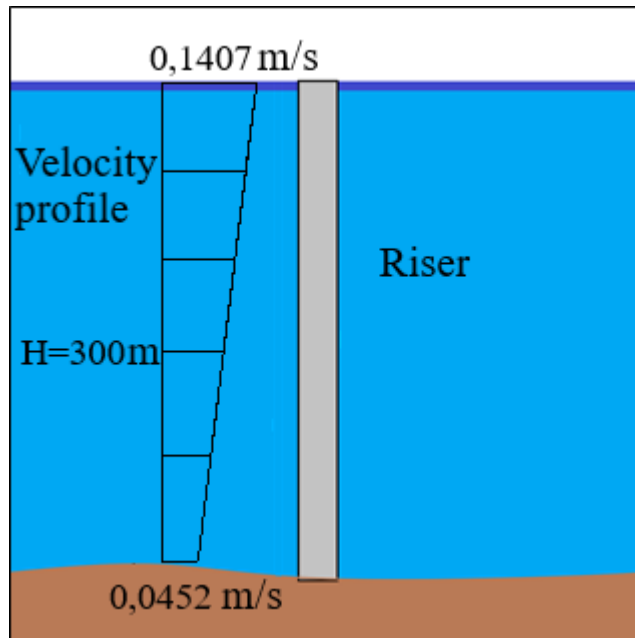


Fig. 6.1. Schematic representation of the task

Since the most common material for risers is X65 steel, when solving the problem, the reference characteristics of this particular steel were taken as the material parameters. A complete table with the input data for the riser is presented in the table 6.2. The American API 5L standard was used in the calculations to determine the pipe diameters.

Table 6.2. Riser parameters

Pipe characteristics:				
Length, L	300	m		
Averaged tension, T	1500	kN	$1,5 \cdot 10^6$	N
Wellhead pressure, P_i	10	MPa	10^7	Pa
Initial inner diameter (API 5L), D_i^*	219,1	mm	0,2191	m
Steel X65 characteristics:				
Yield strength, σ_y	448	MPa	$4,48 \cdot 10^8$	Pa
Young's modulus, E	210	GPa	$2,1 \cdot 10^{11}$	Pa
Steel density, ρ_s			7850	kg/m^3

6.3 Diameters calculation

Let's calculate appropriate diameters for the riser based on an initial internal diameter of 0.2191 m and equilibrium conditions for hoop stress. The external pressure is equal to the hydrostatic seawater:

$$P_o = \rho_{sea\ water} gH = 1025 * 9.81 * 300 = 3,02 \text{ MPa.}$$

Using the formula (5.13), we calculate the minimum proper wall thickness, considering the safety factor $f_1 = 0.72$. Then we calculate the outside diameter and find the closest outside diameter from the table values of the API 5L standard:

$$t^* \geq \frac{(D_i^*)}{2\left(\frac{(f_1\sigma_y + p_i)}{(p_i - p_o)} - 1\right)} = \frac{(0,2191)}{2\left(\frac{(0,72 * 448 * 10^8 + 10^7)}{(10^7 - 3,02 * 10^6)} - 1\right)} = 0,00235 \text{ m} = 2,35 \text{ mm.}$$

$$D_o^* = D_i^* + 2t = 0,2191 + 0,00235 \text{ m} = 0,2238 = 223,8 \text{ mm.}$$

$$D_o(API\ 5L) = 273,1 \text{ mm.}$$

Let's now calculate the optimal wall thickness that meets the yield strength requirements using the formula (5.14) and find the tabular value. Then we calculate the inner diameter using the formula (5.11):

$$t_{opt} \geq \frac{(p_i - p_o)D_o}{2(f_1\sigma_y + p_i)} = \frac{(10^7 - 3,02 * 10^6) * 0,2731}{2(0,72 * 448 * 10^8 + 10^7)} = 0,0029 \text{ m} = 2,9 \text{ mm.}$$

$$t(API\ 5L) = 14,3 \text{ mm.}$$

$$D_i(API\ 5L) = 0.2445 \text{ m} = 244,5 \text{ mm.}$$

Further, having the calculated pipe parameters, we can calculate the natural vibration frequencies and potential response modes.

6.4 Frequency analysis

To begin with, calculate the Reynolds number using formula (3.4) and determine the Strouhal number from the graph in Figure 5.8 for conditions near the seabed and at the surface using the profile of the seawater flow velocity over depth (Figure 1.2). Then, via expression (3.9), calculate the corresponding frequencies of vortex formation.

For surface conditions:

$$Re = \frac{u^{NOB} D_o}{\nu} = \frac{0,1407 * 0,2731}{10^{-6}} = 2,084 * 10^4.$$

$$St = 0,2.$$

$$f_v = \frac{u^{NOB} St}{D_o} = \frac{0,1407 * 0,2}{0,2731} = 0,103 \text{ c}^{-1}.$$

For seabed conditions:

$$Re = \frac{u^{HO} D_o}{\nu} = \frac{0,0425 * 0,2731}{10^{-6}} = 6,7 * 10^3.$$

$$St = 0,2.$$

$$f_v = \frac{u^{HO} St}{D_o} = \frac{0,0425 * 0,2}{0,2731} = 0,033 \text{ c}^{-1}.$$

Then the frequency range of vortex formation varies from 0,033 to 0,103 s⁻¹. Using the boundary values of the interval of dimensionless frequencies [0,125-0,3] and the velocity profile over depth, based on expression (5.4), calculate the range of vibration frequencies:

$$f_{osc} = \frac{\hat{f} * U(H)}{D_o}.$$

$$f_{osc1} = \frac{0,125 * 0,0425}{0,2731} = 0,0207 \text{ s}^{-1}.$$

$$f_{osc2} = \frac{0,3 * 0,0425}{0,2731} = 0,0497 \text{ s}^{-1}.$$

$$f_{osc3} = \frac{0,125 * 0,103}{0,2731} = 0,0644 \text{ s}^{-1}.$$

$$f_{osc4} = \frac{0,3 * 0,103}{0,2731} = 0,1546 \text{ s}^{-1}.$$

Thus, the frequency range of forced oscillations is [0,0207-0,1546]. Now let's move on to calculating natural frequencies for comparison with the obtained range of values. Using formulas (3.7) and (4.4), calculate the total mass per unit length, assume $C_a=1$:

$$\begin{aligned} \bar{m} &= \frac{1}{4} \pi \rho_s (D_o^2 - D_i^2) + \frac{1}{4} \pi \rho_f D_i^2 = \frac{1}{4} \pi (\rho_s (D_o^2 - D_i^2) + \rho_f D_i^2) = \\ &= \frac{1}{4} * 3,14 * (7850 * (0,2731^2 - 0,2445^2) + 600 * 0,2445^2) = 119,4 \text{ kg/m}. \end{aligned}$$

$$\bar{m}_a = \frac{1}{4} C_a \pi \rho_w D_o^2 = \frac{1}{4} * 3,14 * 1025 * (0,2731^2) = 60,04 \text{ kg/m}.$$

$$\bar{m}_t = \bar{m} + \bar{m}_a = 91,27 + 119,4 = 179,48 \text{ kg/m}.$$

The area moment of inertia for a hollow cylinder is calculated by the formula:

$$I = \frac{\pi}{64} (D_o^4 - D_i^4) = \frac{3,14}{64} (0,2731^4 - 0,2445^4) = 9,764 * 10^{-5} \text{ m}^4.$$

Further, based on the equation for calculating the eigenfrequencies corresponding to certain modes (5.3), find the potential modes at which the lock-in conditions may be observed.

The results of calculating the first five natural frequencies are shown in Table 6.3.

Table 6.3. Eigenfrequencies for certain mode

Mode	1	2	3	4	5
$f_{n,tot}$	0,1245	0,2499	0,3769	0,5065	0,6393

From table 6.3, it can be seen that only the first mode is in the desired interval when the riser oscillations may lock on the external influence.

6.5 Cylinder Oscillation Modelling

The flow simulation around the cylinder was performed in the ANSYS STUDENT software. The model of the oscillatory system is described in Chapter 4. During the work, 30 models were calculated to obtain the values of the external forces acting on the cylinder, which will be used to calculate structural dynamics.

6.5.1 Input parameters

The input parameters for the model are the data on the properties of fluids and steel presented in Tables 6.1 and 6.2, the data of the seawater flow velocity profile (Figure 1.4) and the values of mass and natural frequencies calculated in the previous chapter. In addition, the pressure is set equal to the hydrostatic pressure. Also, it is necessary to calculate the coefficient of stiffness of the cylinder (stiffness of the model spring).

The spring stiffness is calculated using formula (4.5) using the lowest natural frequency obtained during frequency analysis (see table 6.3):

$$k = 2 * f_n^2 * \bar{m}_t = 2 * 0,1245^2 * 179,48 = 5,568 \frac{\text{N}}{\text{m}}.$$

Thus, there are all the necessary input parameters for calculating the model.

The URANS equations have been chosen to calculate the flow characteristics. This is because they are the most suitable for solving the problem in this work since the available resources for its implementation are limited, and there is no way to perform calculations using highly demanding models.

The SST k- ω model was chosen as the turbulence model as it allows to make a better description of both the free flow and the flow behavior in the near-wall layer. It is necessary to

accurately determine the external forces acting on the cylinder, which is the main goal of the simulation.

6.5.2 Modelled Domain

The modelling space is represented by a rectangular area representing a certain volume of fluid (Figure 6.2). The fluid domain is 11.1 meters by 8.8 meters. A circle with a smaller radius represents the cylinder wall. The cylinder diameter is equal to the diameter of the riser.

The cylinder is moved closer to the inlet allowing the flow to reach a pseudo-steady state faster. An additional 1-meter radius zone has been added around the cylinder wall to achieve a more detailed description of the fluid behavior and ensure the mesh's motion.

The fluid domain left boundary was set as the inlet from which the stream flows, and the right boundary as the outlet. Thus, the flow is directed from left to right. The upper and lower boundaries are set as symmetry, which allows the flow to move along a boundary freely.

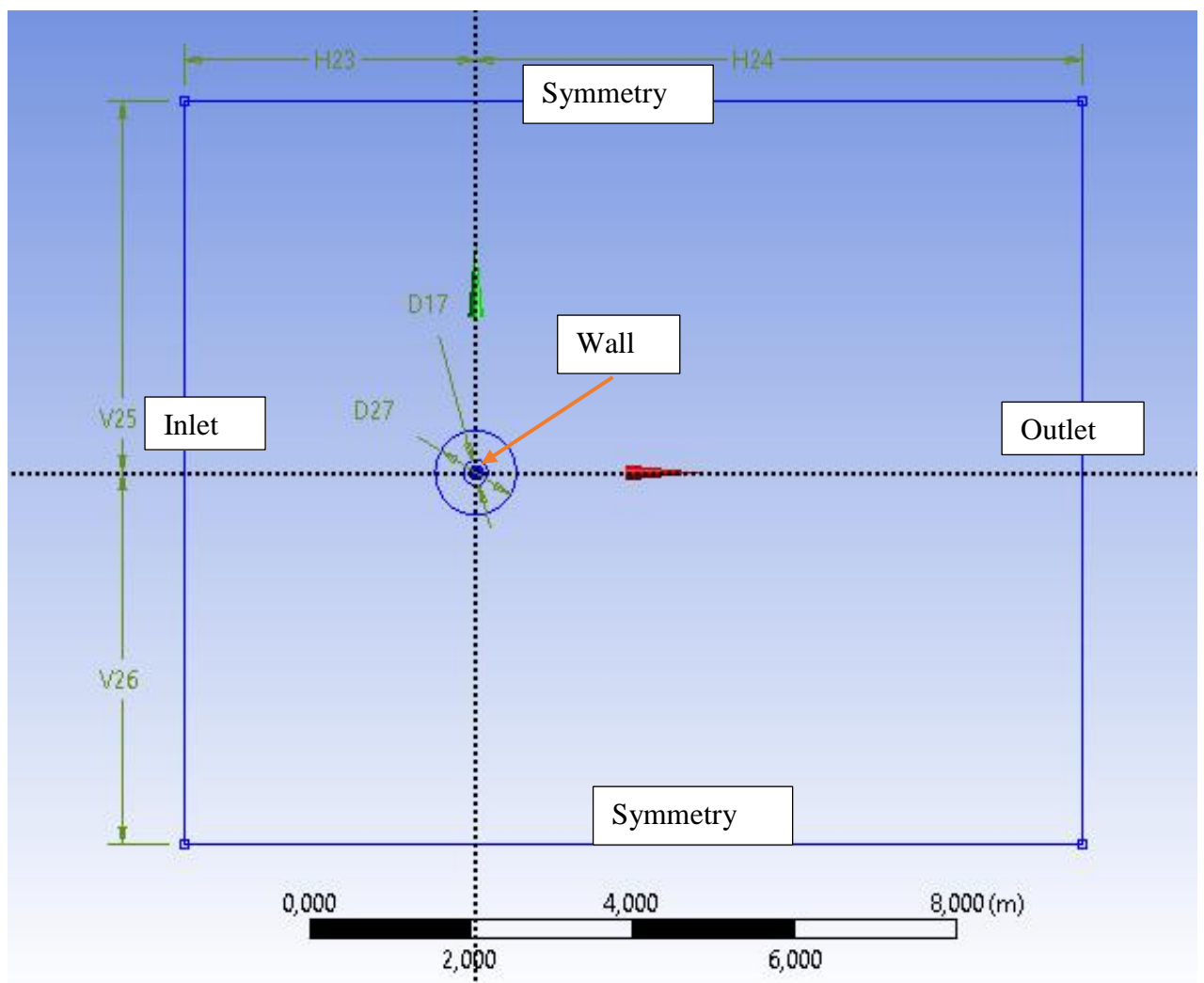


Fig. 6.2. Modelled Domain

The boundary conditions for the simulated space are presented in Table 6.4.

Table 6.4. Boundary conditions for pressure and velocity

Boundary	Boundary condition	
	Velocity	Pressure
Inlet	Set value	Zero gradient
Outlet	Zero gradient	Fixed value
Symmetry	Free	Free
Wall	No-slip	Zero gradient

6.5.3 Mesh Generation

The simulation used an unstructured computational mesh with triangular cells to simplify the recalculation of the dynamic mesh.

The y^+ values for the SST $k-\omega$ turbulence model must be in the range $30 < y^+ < 300$ in order to use the wall function to calculate the parameters near the wall.

For this, we calculate the values of the shear stress rate using the transformation of the logarithmic wall law (2.18):

$$u_*^{\text{поб}} = \frac{u^{\text{поб}}}{2,5 * \ln(5) + 5} = \frac{0,1407}{2,5 * \ln(5) + 5} = 0,0156 \frac{m}{s}$$

$$u_*^{\text{дно}} = \frac{u^{\text{дно}}}{2,5 * \ln(5) + 5} = \frac{0,0452}{2,5 * \ln(5) + 5} = 0,005 \frac{m}{s}$$

The first layer thickness for the mesh is selected based on the formula (2.19). The final value was chosen in such a way that y^+ values for at the surface and seabed conditions satisfy the requirements. The selection results are presented in Table 6.5. It can be seen that the permissible values of the thickness of the first layer of the mesh are in the range [0.01-0.04].

Table 6.5. First layer thickness determination

First layer thickness, m	Y+ (surface)	Y+ (seabed)
0,01	27	84
0,02	54	169
0,03	81	253
0,04	108	338

If to take a value greater than 0.04, then the actual thickness of the near-wall layer will be overestimated for surface conditions. At the same time, considering a value less than 0.01, the calculation of turbulent effects according to the logarithmic law will affect the buffer zone for bottom conditions. Thus, in order to obtain a denser mesh and not distort the result, the calculation of the models was carried out with a first layer thickness value of 0.02.

In order to get a detailed description of distant zones of the near-wall layer, fifteen additional layers were added (Figure 6.3a). The mesh of the zone around the cylinder was improved relative to the rest of the space (Figure 6.3b).

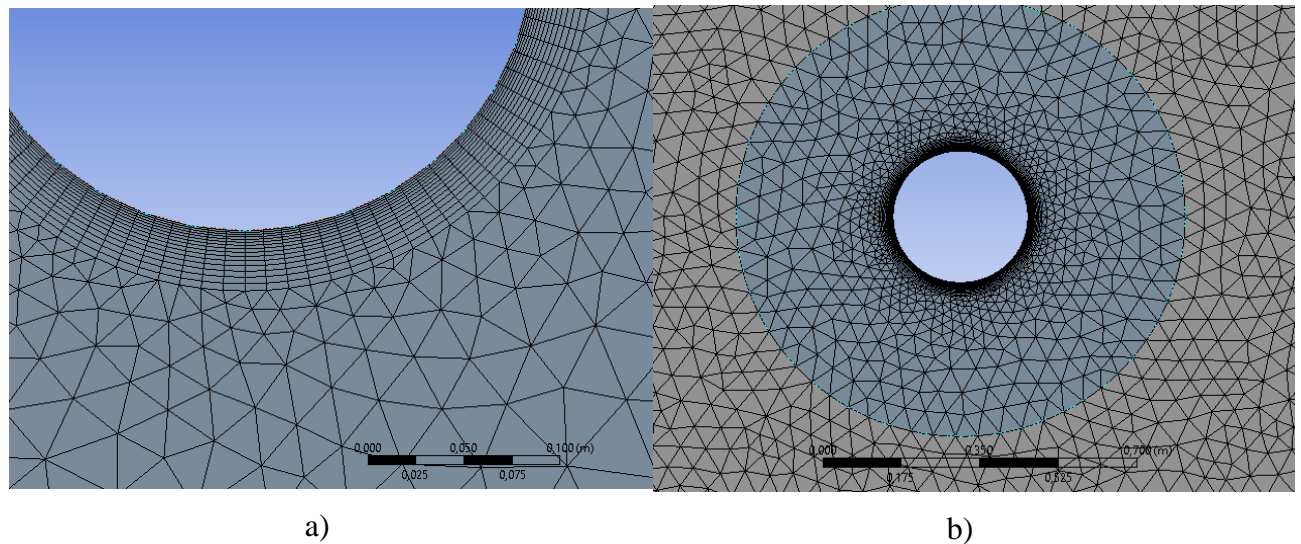


Fig. 6.3. Detailed mesh view: a) in near-wall layer, b) around the cylinder

6.5.4 Modelling Results

In work, 30 model calculations were carried out for different flow rates. However, since the difference in velocities is rather small, and all other input parameters for the models are the same, the flow pattern for currents does not differ significantly.

Figure 6.4 shows vorticity magnitude and streamlines at the first seconds of flow interaction with the cylinder. Seawater current flows around the cylinder on both sides to the wake and creates a force that displaces the cylinder in in-line direction.

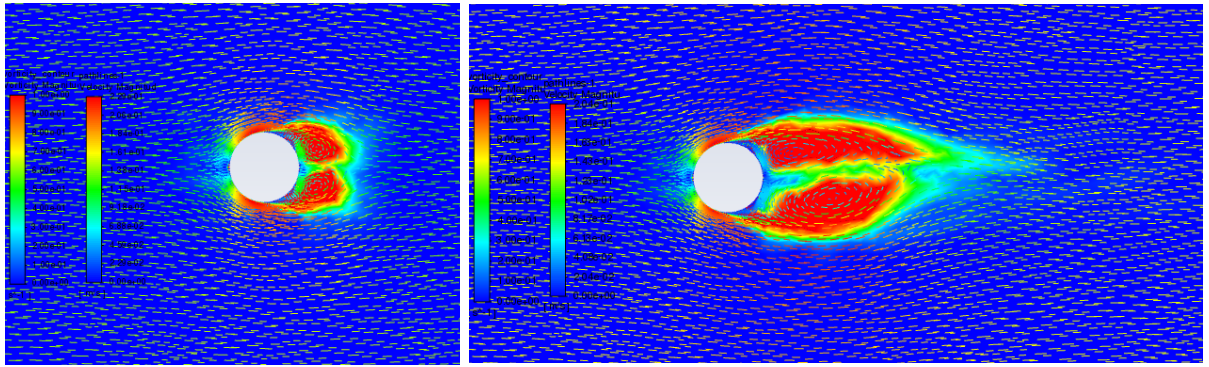


Fig. 6.4. Flow development in the wake

After some time, two zones of increased vortex formation intensity are created behind the cylinder, which transfers energy to neighboring layers. As a result, the vortex formation zones stretch and interact with each other.

At a certain moment in time, one of the zones seems to slide away from the other, cutting it off, leading to the appearance of forces transverse to the main flow acting on the cylinder, which is shown in Figure 6.5.

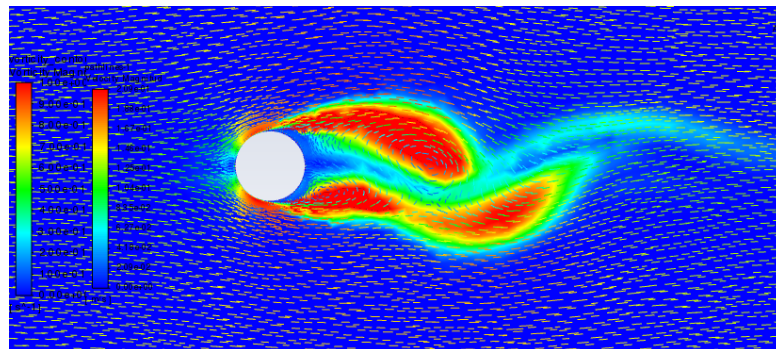


Fig. 6.5. One vorticity zone cuts another

From this moment on, this pattern repeats periodically, forming a system of vortices behind the cylinder. The vortex energy dissipates rather quickly, given the relatively small size of the simulated area. As shown in Figure 6.6, at a distance of about 2.5 meters from the cylinder, vortex flows lose more than half of their intensity.

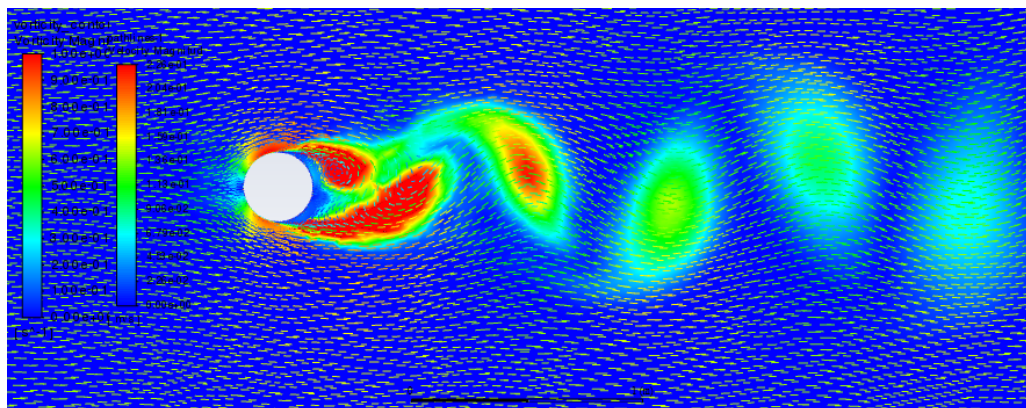


Fig. 6.6. Vorticity intensity dissipation

Since this study is carried out to analyze the forces acting on the cylinder under certain conditions, a comparative analysis of the flow structure for various values of the ratio of the cylinder mass to the displaced water mass, as well as for various values of the superficial velocity, does not make sense. Therefore, at this stage, it remains to represent the velocity field in the vicinity of the cylinder and in the wake (Fig. 6.7) for the surface condition.

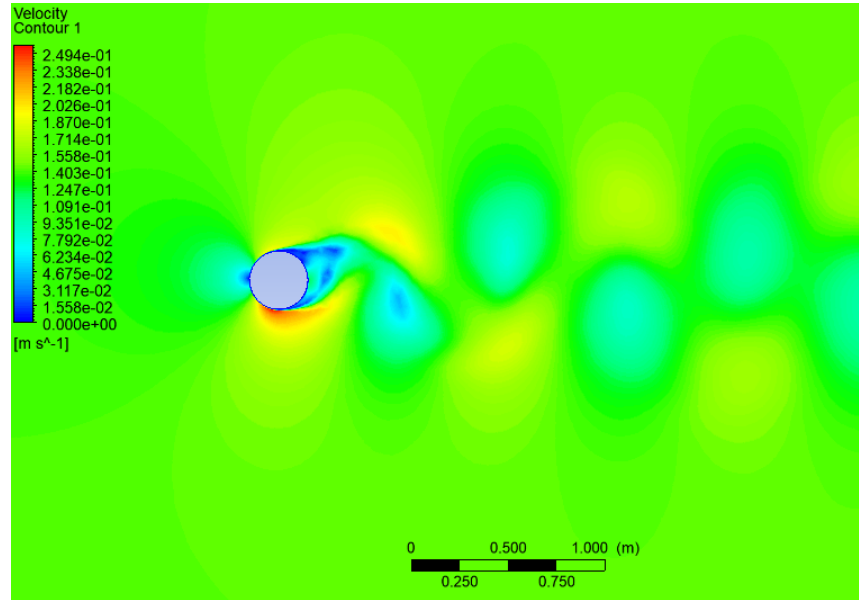


Fig. 6.7. Velocity field around cylinder and in the wake (at surface)

Speaking about the forces, which are called lift and drag forces, the corresponding coefficients are an important characteristic of such forces.

For example, also consider the surface layer, for which the distribution of the lift coefficient is as follows (Figure 6.8).

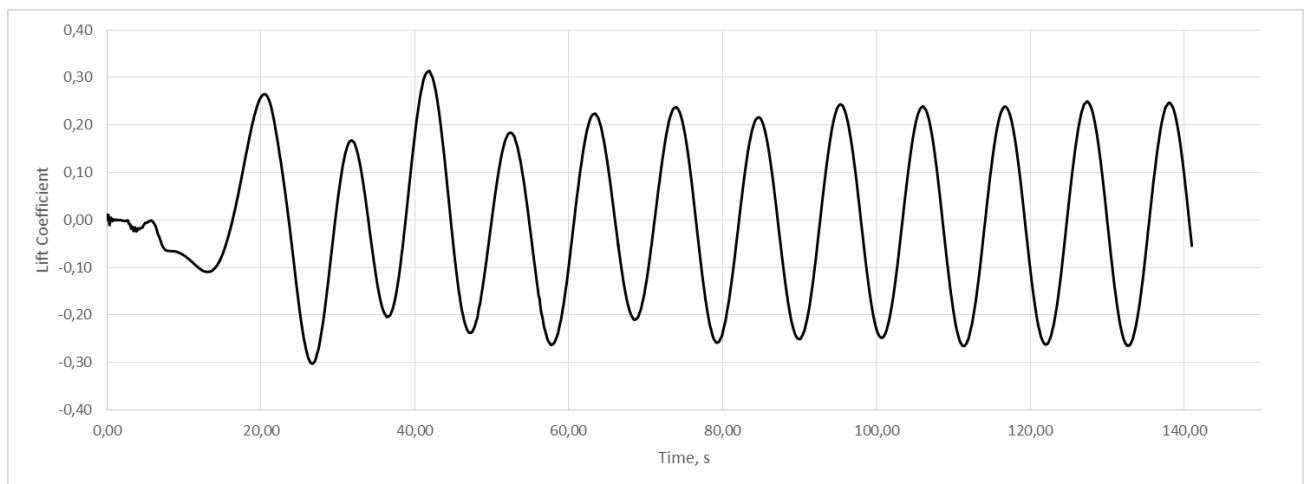


Fig. 6.8. Lift coefficient distribution in time

At first, the oscillations of the cylinder develop rather randomly. The cylinder moves unevenly for the first 60 seconds. Then the system gradually reaches a pseudo-static state when the vibration

amplitudes stabilize at a certain level. For the direction transverse to the flow, oscillations are observed with a frequency of about 11-12 seconds.

The graph of the drag force coefficient (Figure 6.9) is characterized by a sharp increase in the first seconds. However, after this, the values begin to decrease for a while. It corresponds to the moment of the first separation of the vortex behind the cylinder, which can be observed by comparing Figures 6.8 and 6.9.

The cylinder is displaced in the direction of flow. But when the vortex separates, a zone of reduced pressure is created. It contributes to the acceleration of the cylinder in this direction. As a result, frontal loads lose their intensity for a while.

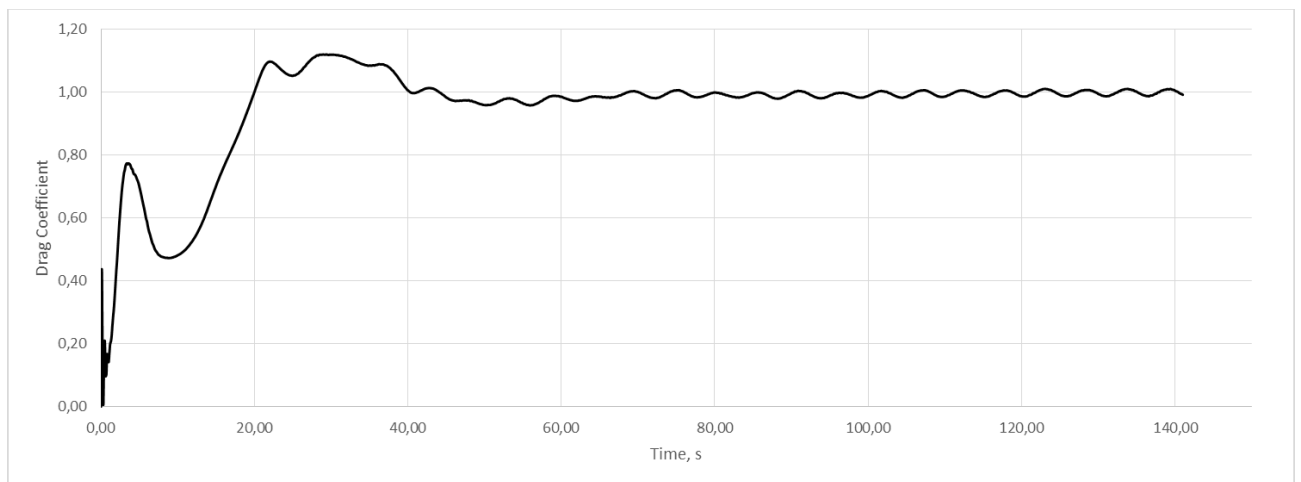


Fig. 6.9. Drag coefficient distribution in time

Further, the frontal loads gradually increase intensity again, and the cylinder's displacement reaches the point of uniform oscillation. As a result, the drag force coefficient is characterized by an oscillation with a frequency of approximately equal to 6 seconds.

This correlates well with the statement in Chapter 5.4.1 that the vibration frequency in the longitudinal direction is usually about twice that in the transverse direction.

6.6 Riser Shape Determination

The input data for performing the structural analysis are the results of the simulation of the flow around the cylinder and the previously calculated cylinder mass per unit length.

From the calculations of each model, the time-distributed values of the force coefficients were derived, which are then used to calculate the values of the forces themselves using equations (3.2), (3.3).

The approach to determining the shape of the riser is described in Chapter 5.2, where it is also indicated that the solution of the equations of motion can be obtained using two methods. In this work, the discrete implicit scheme of the Newmark beta method was used. The system of discrete equations for each coordinate has the following form:

$$\begin{cases} M\ddot{u}_i + c\dot{u}_i + ku_i = F_i \\ u(t_0) = u_0, \quad \dot{u}(t_0) = \dot{u}_0 \end{cases} \quad (6.1)$$

$$\begin{cases} u_{i+1} = u_i + \dot{u}_i\Delta t + \ddot{u}_i\left(\frac{1}{2} - \beta\right)\Delta t^2 + \ddot{u}_{i+1}\beta\Delta t^2, \\ \dot{u}_{i+1} = \dot{u}_i + \ddot{u}_i(1 - \gamma)\Delta t + \ddot{u}_{i+1}\gamma\Delta t \end{cases}, \quad (6.2)$$

where: Δt – time step;

$u_i, \dot{u}_i, \ddot{u}_i$ – displacement, velocity and acceleration at i time step;

$u_{i+1}, \dot{u}_{i+1}, \ddot{u}_{i+1}$ – displacement, velocity and acceleration at $i+1$ time step;

$$\beta = \frac{1}{4}, \gamma = \frac{1}{2}.$$

The parameters β and γ are set by Newmark himself to achieve the unconditionally stable solution for any input data.

It is also required some additional calculations to solve the system. So, at the first stage, additional coefficients are introduced to simplify the further representation of the equations:

$$\begin{aligned} a_0 &= \frac{1}{\beta\Delta t^2}, & a_1 &= \frac{\gamma}{\beta\Delta t}, & a_2 &= \frac{1}{\beta\Delta t}, & a_3 &= \frac{\gamma}{2\beta} - 1, & a_4 &= \frac{\gamma}{\beta} - 1, \\ a_5 &= \frac{\Delta t}{2}\left(\frac{\gamma}{\beta} - 2\right), & a_6 &= \Delta t(1 - \gamma), & a_7 &= \gamma\Delta t. \end{aligned}$$

The calculation starts from the setup of initial conditions. Then the acceleration is calculated from the equation of motion (6.1) and the effective stiffness matrix, which also simplifies further writing:

$$\ddot{u}_0 = M^{-1}(F_0 - Ku_0 - C\dot{u}_0), \quad (6.3)$$

$$K_e = K + a_0M + a_1C, \quad (6.4)$$

Now, having all the values for the initial conditions, calculate the required parameters at the next time step:

$$F_e = F_{i+1} + M(a_0 u_i + a_2 \dot{u}_i + a_3 \ddot{u}_i) + C(a_1 u_i + a_4 \dot{u}_i + a_5 \ddot{u}_i), \quad (6.4)$$

$$u_{i+1} = K_e^{-1} F_e, \quad (6.5)$$

$$\ddot{u}_{i+1} = a_0 (u_{i+1} - u_i) - a_2 \dot{u}_i - a_3 \ddot{u}_i, \quad (6.6)$$

$$\dot{u}_{i+1} = \dot{u}_i + a_6 \ddot{u}_i + a_7 \dot{u}_i, \quad (6.7)$$

The solution of the discrete scheme was carried out using the mathematical package Matlab.

Thus, having performed calculations of a discrete scheme on 30 riser sections, it is possible to obtain a dynamic picture of the behavior of the entire riser as a whole.

The resulting riser profiles correlate with modal analysis data, as seen in Figure 6.10a, which shows the riser displacement with water depth. The riser shape is very similar to the first mode. It can also be noted that the fast surface currents have a greater impact, as evidenced by the more intense displacement at depths of fewer than 150 meters.

For displacements perpendicular to the flow (Figure 6.10b), a different picture is observed, and most likely, it is caused by vortex formation on the pipe wall. The riser profile is quite unstable. It constantly experiences wave-like fluctuations.



Fig. 6.10. Riser displacement in direction: a) in-line (X) and b) cross-flow (Y)

6.7 Bending Stress Calculation

Since the X and Y offset values of the riser along the Z axis are known, the zone of greatest curvature can be found. The greatest curvature will correspond to the profile characterized by large values of the mode. This is because high values of the mode have a denser distribution of waves along the length of the pipe and, therefore, intense bending.

The greatest curvature corresponds to the point where the profile has the smallest radius. The point of the smallest radius can be determined by three points approach if they are all at the same distance from each other along the Z axis. For this, the expression of a circular arc is used, where its value is approximated through three points. Thus, it is determined that the minimum bending radius is at a depth of 70 meters.

Since the riser bends little at small distances, the approximated arc length can be calculated as the real one with an error. Considering all the above find the minimal radius of curvature:

$$R_{min} = \frac{c}{2\pi}, = \frac{808,48}{2 * 3,14} = 128,74 \text{ m}$$

Then, using formulas (7.19), (7.20), calculate the relative deformation at this point:

$$\varepsilon_{max} = \frac{D_o}{2R_{min}} = \frac{0,2731}{2*128,74} = 106 * 10^{-5}.$$

$$\sigma_{max} = E\varepsilon_{max} = 106 * 10^{-5} * 2,1 * 10^{11} = 222,6 * 10^6 \text{ Pa}.$$

The maximum stress is significantly less than the yield point of the material. Thus it can be concluded that this type of riser is safe for the given conditions.

Discussion

The studies and calculations carried out in work showed that for the conditions of the South Barents Basin of the Barents Sea, the use of top tension risers at depths in the region of 300 meters is quite safe, given the similarity of the pipe and material parameters with those presented in this work. Furthermore, the displacement amplitudes under such conditions do not lead to an excess of the permissible voltage values.

In general, the results presented in work can be the basis for further, more detailed calculations for the conditions of the Barents Sea.

However, it should be noted that the study did not consider the oscillatory movements of the platform on the surface and wave loads. Also, the inertial forces of the internal flow were not taken into account.

Another important aspect is the choice of pipe material, as material changes can lead to completely different dynamic behavior.

However, despite the permissible load values, cyclic vibrations of the riser in the lateral flow direction and undulating movements can cause additional fatigue stresses.

The simulation of cylinder vibrations performed during the work showed that vibrations could occur even at low flow rates. Such vibrations can be low-amplitude, but they can also be synchronized with the structure.

For the riser studied in work, no synchronization of natural frequencies with the frequencies of external influence was observed. Apparently, the influence of the added mass and the velocity gradient along the depth contribute to the frequency characteristics change. The influence of these factors can shift the phases of oscillatory movements in such a way that the lock-in conditions cannot be observed for a long time but occurs only in a limited interval.

It is necessary to carry out a sufficiently long simulation in the range of 1000 seconds to study such a problem in more detail. Such time scales will allow seeing how stable the process of vortex formation is.

In this study, the models were calculated until a pseudo-stationary regime was obtained. The time intervals were about 150 with a maximum of 200 seconds.

The amplitudes of displacement in the direction of the transverse flow were no more than 0.4 m, which is quite acceptable given that this value refers to mode 1, which means that the bending stress is distributed over the entire length of the pipe.

Longitudinal displacements are characterized by maximum values in the region of 0.1 m, which is also not critical or dangerous.

The calculations were based on the multi-strip method, which has proven itself an alternative to resource-intensive and more complex methods for solving such a problem, for example, complex 3D fluid-structure interaction modelling.

When considering many 2D problems, it also needs sufficient computational power and a lot of time. But since space is studied only in two coordinates, the problem is highly simplified. As a result, it makes it much easier both to create a computational grid and achieve the solution's convergence.

In turn, the mathematical representation of the structural dynamics to the same extent allows performing all the necessary calculations based on the values obtained in the simulation and obtaining a satisfactory result.

Bibliography

1. Achenbach E., Heinecke E. On vortex shedding from smooth and rough cylinders in the range of Reynolds numbers 6×10^3 to 5×10^6 . *Journal of Fluid Mechanics*, 1981, vol. 109, pages 239-251. doi.org/10.1017/S002211208100102X
2. API 5L. Specification for Line Pipe. Forty-Sixth Edition. 2018 // API Web Store site. – URL: <https://www.apiwebstore.org/publications/item.cgi?eddfb1d2-8077-428a-82ce-3fd0a26ba415>
3. Bredberg J. On the Wall Boundary Condition for Turbulence Models. Department of Thermo and Fluid Dynamics, Chalmers University of Technology, 2000.
4. Catalano P., Wang M., Iaccarino G., Moin P. Numerical simulation of the flow around a circular cylinder at high Reynolds numbers. *International Journal of Heat and Fluid Flow*, 2003, vol. 24, issue 4, ppages 463-469. [doi.org/10.1016/S0142-727X\(03\)00061-4](https://doi.org/10.1016/S0142-727X(03)00061-4)
5. Çengel Y. A. and Cimbala J. M. *Fluid Mechanics: Fundamentals and Applications* 3rd Edition. McGraw-Hill Higher Education, 2010.
6. Constantinides Y., Oakley O.H. Numerical Prediction of Bare and Straked Cylinder VIV. *Proceedings of the 25th International Conference on Offshore Mechanics and Arctic Engineering*. 2006, vol 4, pages 745-753. doi.org/10.1115/OMAE2006-92334
7. Duan M., Wan D., and Hongxiang X. Prediction of Response for Vortex-Induced Vibrations of a Flexible Riser Pipe by using Multi-Strip Method. *The 26th International Ocean and Polar Engineering Conference*, 2016
8. Fröhlich J, von Terzi D. Hybrid LES/RANS methods for the simulation of turbulent flows. *Progress in Aerospace Sciences*, 2008, vol. 44, pages 349–377.
9. Gabbai R.D., Benaroya H. A first-principles derivation procedure for wake-body models in vortex-induced vibration: Proof-of-concept. *Journal of Sound and Vibration*, 2008, vol. 312, issues 1–2, pages 19-38, doi.org/10.1016/j.jsv.2007.07.086
10. Germano M, Piomelli U, Moin P, Cabot WH. A dynamic subgrid-scale eddy viscosity model. *Physics of Fluids A: Fluid Dynamics*, 1991, vol. 3. Pages 1760–1765. <https://doi.org/10.1063/1.20857955>
11. Govardhan, R., Williamson, C. Modes of vortex formation and frequency response of a freely vibrating cylinder. *Journal of Fluid Mechanics*, 2000, vol. 420, pages 85-130. doi.org/10.1017/S0022112000001233
12. Heng X., Paola C. Quantification of model uncertainty in RANS simulations: A review. *Progress in Aerospace Sciences*, 2019, vol. 108, pages 1-31. doi.org/10.1016/j.paerosci.2018.10.001.

13. Jiang, H., & Cheng, L. Strouhal–Reynolds number relationship for flow past a circular cylinder. *Journal of Fluid Mechanics*, 2017, vol. 832, pages 170-188. doi.org/10.1017/jfm.2017.685
14. Jimin He, Zhi-Fang Fu. 1 – Overview of modal analysis / *Modal Analysis*. Butterworth-Heinemann, 2001, pages 1-11. doi.org/10.1016/B978-075065079-3/50001-2
15. Karim M., Rahman M.M., Alim M. A. Numerical computation of viscous drag for axisymmetric underwater vehicles. *Jurnal Mekanikal*, 2008, vol. 26, pages 9-21.
16. Karunakaran D. N. OFF520 “Pipelines and risers” course materials. University of Stavanger, 2020.
17. Kim I. and Wu X. L. Unified Strouhal-Reynolds number relationship for laminar vortex streets generated by different-shaped obstacles. *American Physical Society*, 2015. doi.org/10.1103/PhysRevE.92.043011
18. Larsen C.M., Baarholm G.S., Lie H. On fatigue damage accumulation from in-line and cross-flow vortex-induced vibrations on risers. *Journal of Fluids and Structures*, 2006, vol. 22, issue 1, pages 109-127. doi.org/10.1016/j.jfluidstructs.2005.07.013
19. Lie H., Kaasen K.E. Modal analysis of measurements from a large-scale VIV model test of a riser in linearly sheared flow. *Journal of Fluids and Structures*, 2006, vol. 22, issue 4, pages 557-575. doi.org/10.1016/j.jfluidstructs.2006.01.002
20. Menter F.R. Two-Equation Eddy-Viscosity Turbulence Models for Engineering Applications. *AIAA Journal*, 1994, vol. 32, pages 1598-1605.
21. Muk C. O. OFF600 “Marine Operations” course materials. University of Stavanger, 2020.
22. Orszag S. Analytical theories of turbulence. *Journal of Fluid Mechanics*, 1970, vol. 41, pages 363-386. [doi:10.1017/S0022112070000642](https://doi.org/10.1017/S0022112070000642)
23. Park S. B., Shin S. Y., Shin D. G., Jung K. H., Choi Y. H., Lee J. and Lee S. J. Extreme Value Analysis of Metocean Data for Barents Sea. *Journal of Ocean Engineering and Technology*, 2020, vol. 34, pages 26-36. doi.org/10.26748/KSOE.2019.094
24. Qiang B, Yong B. 1 – Introduction. *Subsea Pipeline Design, Analysis, and Installation*. Gulf Professional Publishing, 2014, pages 3-21. doi.org/10.1016/B978-0-12-386888-6.00001-8
25. Schmitt F. G. About Boussinesq's turbulent viscosity hypothesis: historical remarks and a direct evaluation of its validity. *Comptes Rendus Mécanique*, 2007, vol. 335, issues 9–10, pages 617-627, doi.org/10.1016/j.crme.2007.08.004
26. Schulz, K.W., Meling, T.S. Multi-Strip Numerical Analysis for Flexible Riser Response. *Proceedings of the ASME 2004 23rd International Conference on Offshore Mechanics and Arctic Engineering*, 2004, vol. 1, parts A and B, pages 379-384. doi.org/10.1115/OMAE2004-51186

27. Spalart PR. Detached-eddy simulation. Annual Review of Fluid Mechanics, 2009, vol. 41, pages 181– 202.
28. Sumer B., Fredsoe J. Hydrodynamics around Cylindrical Structures, 2006
29. Wilcox DC. Turbulence modeling for CFD. DCW Industries, third edition, 2006.
30. Williamson, C. Oblique and parallel modes of vortex shedding in the wake of a circular cylinder at low Reynolds numbers. Journal of Fluid Mechanics, 1989, vol. 206, pages 579-627. [doi:10.1017/S0022112089002429](https://doi.org/10.1017/S0022112089002429)
31. Wu J., Yin D., Lie H., Larsen C. M., Baarholm R. J., and Liapis S. On the Significance of the Higher-Order Stress in Riser Vortex-Induced Vibrations Responses. Journal of Offshore Mechanics and Arctic Engineering, 2019. doi.org/10.1115/1.4040798
32. Yong Bai, Qiang Bai. 30 – Subsea Production Risers. Subsea Engineering Handbook (Second Edition). Gulf Professional Publishing, 2019, pages 885-918. doi.org/10.1016/B978-0-12-812622-6.00030-0
33. Zahari M.A., Dol S.S. Effects of Different Sizes of Cylinder Diameter on Vortex-Induced Vibration for Energy Generation. Journal of Applied Sciences, 2015, vol. 15, pages 783-791. doi.org/10.3923/jas.2015.783.791
34. Zhao M., Cheng L. Vortex-induced vibration of a circular cylinder of finite length. Physics of Fluids, 2013, vol. 26. doi.org/10.1063/1.4862548
35. ГОСТ 33005-2014 (ISO 13625:2002). Межгосударственный стандарт. Нефтяная и газовая промышленностью Оборудование буровое и эксплуатационное. Соединения морских буровых райзеров Общие технические требования. [Электронный ресурс] // Электронный фонд правовых и нормативно-технических документов. URL: <https://docs.cntd.ru/document/1200123726> (дата обращения: 03.05.2021).
36. ГОСТ Р 54382. Нефтяная и газовая промышленность. Подводные трубопроводные системы. Общие технические требования. [Электронный ресурс] // Электронный фонд правовых и нормативно-технических документов. URL: <https://docs.cntd.ru/document/1200086533> (дата обращения: 03.05.2021).
37. Григоренко Ю. Н., Маргулис Л. С., Новиков Ю. Н., Соболев В. С. / Морская база углеводородного сырья России и перспективы ее развития // Нефтегазовая геология. Теория и практика. – 2007. – т. 2. URL: <http://ngtp.ru/rub/5/003.pdf>
38. Кульпин Л.Г., Шевчук В.В., Зимин А.Д. / Предварительные предложения по использованию ближайших месторождений Баренцева моря для газификации района г. Мурманска. // V-я международная конференция «Освоение Арктического шельфа: шаг за шагом». Ассоциация «Мурманшельф», 2012. URL: <http://www.murmanshelf-conf.ru/archive/files/2012/kulpin.pdf>